remote sensing

MDPI

Article

A Study on Brightness Reversal of Internal Waves in the Celebes Sea Using Himawari-8 Images

Beilei Hu [1,2], Junmin Meng [1,2,*], Lina Sun [1,2] and Hao Zhang [1,2]

1 First Institute of Oceanography, Ministry of Natural Resources, Qingdao 266061, China; hubeilei@fio.org.cn (B.H.); sunln@fio.org.cn (L.S.); zhanghao@fio.org.cn (H.Z.)
2 Technology Innovation Center for Ocean Telemetry, Ministry of Natural Resources, Qingdao 266061, China
* Correspondence: mengjm@fio.org.cn

Abstract: A geostationary meteorological satellite is located at a fixed point above the equator, which can continuously observe internal waves and provides great advantages in research on changes in the generation and propagation of internal waves. The scale of internal waves in the Celebes Sea is large, which is still very obvious in geostationary meteorological satellite images with a lower spatial resolution. This study considers continuous remote sensing images of geostationary meteorological satellite Himawari-8 to analyze the bright and dark features of internal waves in the Celebes Sea in optical remote sensing images. The solar zenith angle, sensor zenith angle and relative azimuth angle of internal waves in six images are calculated, and the changes are 12.45°, 0.20° and 3.44°, respectively, within 50 min. Moreover, based on the normalized sunglint radiance theory, the critical solar viewing angle is proposed and verified. The results indicate that the bright and dark features of internal waves when passing through sunglint and non-sunglint areas are greatly reversed, and the critical solar viewing angles are 18.73° and 27.41°, respectively. In this study, geostationary meteorological satellite Himawari-8 images are analyzed to study on the brightness reversal phenomenon of internal waves for the first time, and a unique brightness change in internal waves during the propagation process is revealed, which has not been reported in existing research.

Keywords: internal waves; Himawari-8; brightness reversals; critical solar viewing angle; sunglint

check for updates

Citation: Hu, B.; Meng, J.; Sun, L.; Zhang, H. A Study on Brightness Reversal of Internal Waves in the Celebes Sea Using Himawari-8 Images. *Remote Sens.* **2021**, *13*, 3831. https://doi.org/10.3390/rs13193831

Academic Editor: Weimin Huang

Received: 22 August 2021
Accepted: 20 September 2021
Published: 24 September 2021

1. Introduction

Internal waves are a widely occurring phenomenon in global oceans under stable density stratification. Due to the corresponding strong vertical and horizontal currents, they pose hazards to the safety of ship navigation and nutrient supply for photosynthesis, sediment and pollutant transport, acoustic transmission, etc. [1,2]. Therefore, the study of ocean internal waves has scientific and engineering significance.

The application of remote sensing satellite images to observe internal waves is one of the mainstream methods to study the characteristics of internal waves [3]. Propagation of internal waves modulates microscale waves on the sea surface, leading to local changes in the sea surface roughness, while convergence and divergence zones can be formed, which comprises the physical basis for remote sensing observations of internal waves [4,5]. Optical remote sensing images are widely implemented in internal wave detection due to their advantages of wide coverage, and low cost of use. Optical remote sensing relies on specular reflection or nearly specular reflection to achieve imaging. Changes in the surface roughness caused by internal waves affect the angles of the sea surface facet tilt, thereby changing the position of the specular reflection area or nearly specular reflection area in a given image [6]. Therefore, in optical remote sensing images, internal waves usually appear as bright-dark or dark-bright bands at a certain gradient, mainly in the specular reflection area or nearly specular reflection area, also referred to as sunglint [7]. Internal waves at different sunglint positions in the same remote sensing image exhibit distinct bright and dark features, and internal waves at the same position also exhibit different bright and dark features at various times [8,9]. This suggests that the bright and dark features of internal waves observed in various sunglint images are very different. The bright and dark features of internal waves represent an important basis for the inversion of internal wave characteristic parameters based on optical remote sensing images, so it is crucial to accurately determine the bright and dark features of internal waves in optical remote sensing images. Moreover, sunglint is the main factor influencing the changes in the bright and dark features of internal waves.

By studying the whole process of sunglint radiance on the sea surface, the bright and dark features of internal waves in optical satellite images can be understood more deeply. Cox and Munk derived a mathematical expression of the specular or nearly specular solar radiance reflected by the sea surface [10]. Saunders estimated the sea surface radiance under the conditions of incorporating shadowing and multiple scattering [11]. Chapman proposed the root mean square slope of the sea surface to describe the relative visibility of ocean surface disturbances [12]. Zeisse analyzed the relationship of the distribution of the capillary wave slope on the sea surface with sunglint [13]. Matthews established a geometric model of sunglint observation considering Advanced Spaceborne Thermal Emission and Reflection Radiometer (ASTER) stereo image pairs and combined ASTER and Landsat images to analyze the characteristics of internal waves in the Strait of Gibraltar [14]. Jackson found that at a specific sensor zenith angle, the bright and dark bands of internal waves in Moderate Resolution Imaging Spectroradiometer (MODIS) images were reversed, thus introducing the concept of the critical sensor viewing angle [15]. Zhang determined that the same internal wave detected by MODIS and Ocean and Land Color Imager (OLCI) did not reveal the same bright and dark features and found that the reason for this phenomenon was the 12.6° rotation of the OLCI camera to the west [16]. From an experimental point of view, Zhang observed that the bright and dark bands of a given internal wave were reversed in the sink when the zenith angle of the light source reached 64.90° and verified the occurrence of the critical sensor viewing angle based on MODIS images [8].

The abovementioned studies on the changes in the bright and dark features of the sea surface are all based on polar-orbiting satellite sensors, but continuous sea surface observation is impossible due to the low temporal resolution. As a dynamic phenomenon, the bright and dark features of internal waves in remote sensing images change continuously, and therefore, a high temporal resolution of the satellite sensor is required. Geostationary meteorological satellites exhibit the advantage of a high temporal resolution and continuous observations, which can mitigate the shortcomings of polar-orbiting satellites, and these satellites can acquire long time series of remote sensing images to observe the changes in bright and dark features of internal waves during propagation.

The main geostationary meteorological satellites currently in service include GOES-16, Meteosat-5, Himawari-8, and FY-4A. These satellites provide large and continuous remote sensing images that can be applied in internal wave observations. Antonio first adopted MeteoSat-5 sunglint imagery in the western Mascarene Ridge area of the western Indian Ocean to demonstrate the potential of geostationary satellites for internal wave monitoring [17]. Lindsey employed geostationary satellite Himawari-8 imagery to track nonlinear internal waves in Indonesian seas and calculated the speed and wavelength of internal waves [18]. Gao applied Himawari-8 imagery in the South China Sea and found that the properties of internal solitary waves (ISWs) during propagation are not stable and remain nonlinear throughout their lifetime [19]. Kurang analyzed the generation and propagation of internal waves in the Flores Sea using Himawari-8 geostationary satellite images and estimated the important parameters related to the propagation of ISWs, further revealing the refraction and reflection of internal waves [20]. Ma compared FY-4A and MODIS remote sensing images and found that FY-4A data are suitable for internal wave observations and calculated the speed of internal waves [21].

Therefore, this paper analyzes the process of the change in the bright and dark features of internal waves in Himawari-8 satellite images. First, we calculate the solar and sensor zenith angles and relative azimuth angle of the internal waves observed in every image. Then, we evaluate the changes in these angles at 10 min intervals. Finally, we examine and confirm the critical solar viewing angle affecting the brightness reversal process of internal waves. This work aims to provide a new idea to study the reasons for the different bright and dark features of internal waves in various remote sensing images.

2. Area and Data

2.1. Area

The Celebes Sea is one of the areas where high-frequency internal waves occur, which is connected to the Sulu Sea and Java Sea. The width from east to west is approximately 840 km, and the width from north to south reaches approximately 520 km. The Celebes Sea covers an area of 435000 km^2, and the average water depth is 4000 m (Figure 1). The climate in the Celebes Sea is controlled by the tropical monsoon climate, and there are only two seasons throughout the year, namely, rainy summer and dry winter seasons [22,23]. The freely interconnected marine waters across a sharply varied topography produce semidiurnal internal waves under the influence of the barotropic tidal force in the Celebes Sea [24]. The internal waves in the Celebes Sea exhibit a large scale and mainly propagate southward toward the coast of Indonesia, and a small fraction of these waves propagate westward [25,26]. Figure 1 also represents the spatial distribution characteristics of internal waves in Celebes Sea. The internal waves in Figure 1 are extracted from the 111 optical images obtained by Moderate-resolution Imaging Spectroradiometer (MODIS) mounted on Terra and aqua satellites from 2017 to 2018, which the spatial resolution is 250m and the band are 0.64 and 0.85 μm. These optical images have undergone geometric correction and projection conversion processing. It should be noted that the internal waves in Figure 1 is actually the crest line of the internal waves in the MODIS image.

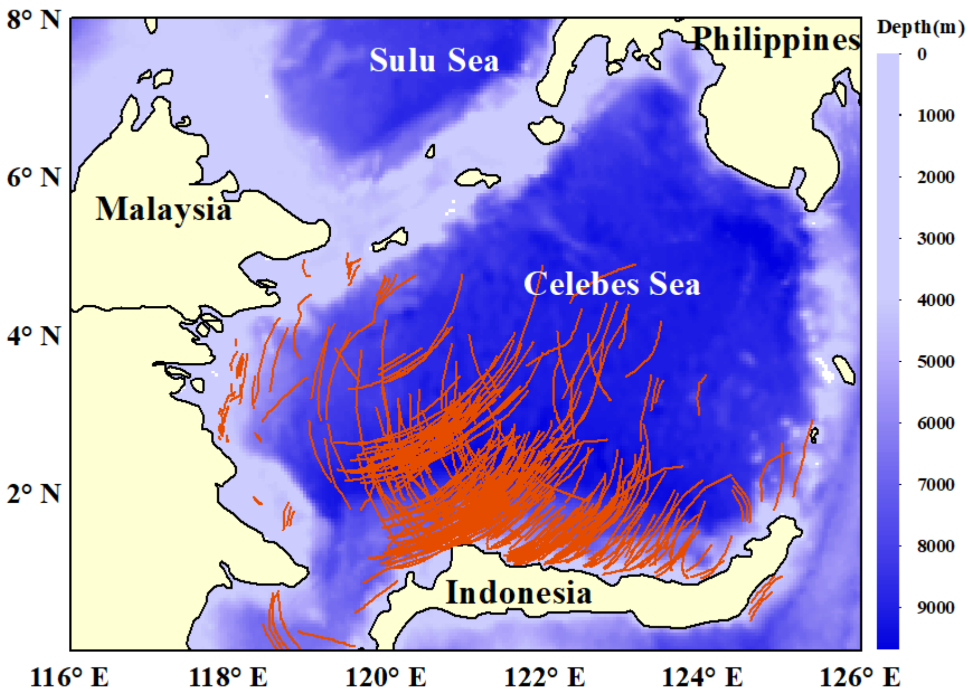

Figure 1. Spatial distribution of internal waves in the Celebes Sea, which are extracted from MODIS images from 2017–2018.

2.2. Data Source

The remote sensing satellite considered in this study is the new geostationary meteorological satellite Himawari-8, which was launched by the Japanese Meteorological Agency (JMA) on 7 October 2014, and the Himawari-8 satellite has been located above the equator at 140.7°E [27]. The Advanced Himawari Imager (AHI) carried by the Himawari-8 satellite provides 16 bands, but the spatial resolution of each band in images is not consistent. The AHI can generate a full disk image at intervals of 10 min, two Japanese regional images and target area images at intervals of 2.5 min, and landmark area images every 0.5 min [28]. Determining the position of an internal wave on the Himawari-8 satellite image will caused an error of 0.5 pixel, but this error does not affect the bright and dark features of the internal wave.

Figure 2 shows a Himawari-8 visible band full disk image of the Celebes Sea recorded on 20 September 2020 at 05:20 UTC. The image contains four solitons in the Celebes Sea that propagate toward the coast of Indonesia. The signatures of internal waves in the Himawari-8 image are distinct, which indicates that the application of Himawari-8 images to observe the features of internal waves in the Celebes Sea is more than sufficient.

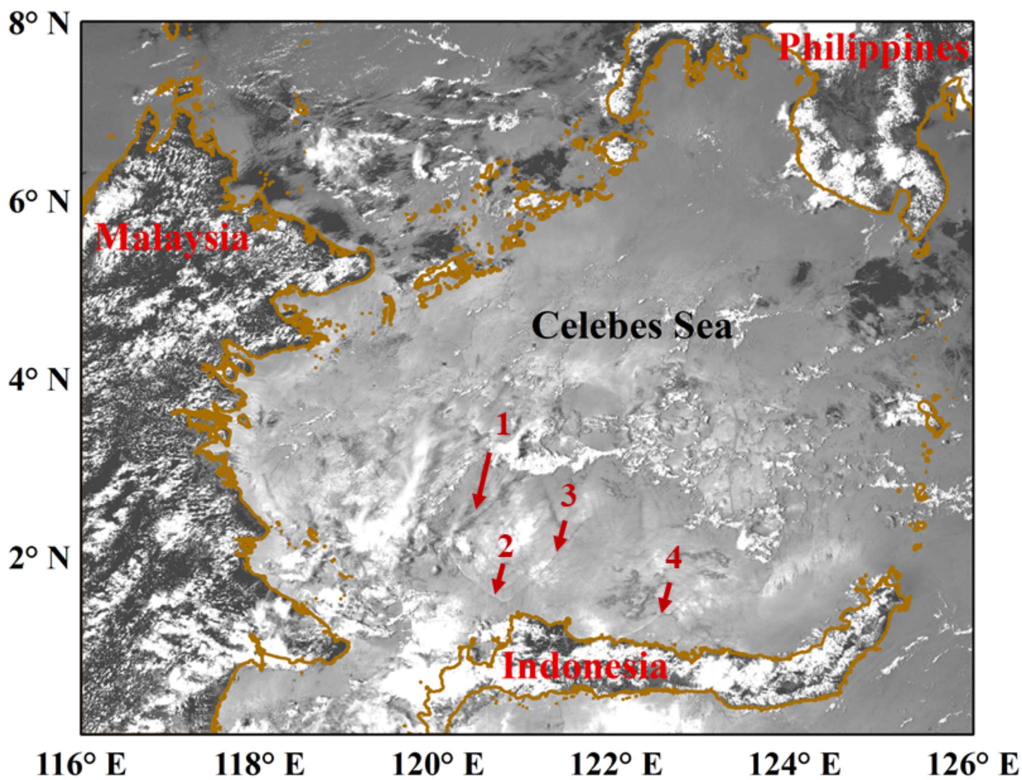

Figure 2. Himawari-8 visible band full disk image of the Celebes Sea on 20 September 2020 at 05:20 UTC. Four solitons occur in the image that propagate toward the coast of Indonesia.

Details of the Himawari-8 images applied in this paper are presented in Table 1.

Table 1. Basic information of the 6 Himawari-8 images.

Name	Time (UTC)
HS_H08_20200921_0450_B03_FLDK_R05_S0510	2020-09-21-04:50
HS_H08_20200921_0500_B03_FLDK_R05_S0510	2020-09-21-05:00
HS_H08_20200921_0510_B03_FLDK_R05_S0510	2020-09-21-05:10
HS_H08_20200921_0520_B03_FLDK_R05_S0510	2020-09-21-05:20
HS_H08_20200921_0530_B03_FLDK_R05_S0510	2020-09-21-05:30
HS_H08_20200921_0540_B03_FLDK_R05_S0510	2020-09-21-05:40

2.3. Data Preprocessing

The full disk images applied in this paper exhibit a spatial resolution of 500 m and a temporal resolution of 10 min with a center wavelength of 0.64 µm [29]. Each full disk image is stored as 10 DAT files in the Himawari Standard Data (HSD) format. The data in this format comprise 12 blocks, where the top 11 blocks are header blocks and the last block is an image block [29]. The preprocessing steps of these images include raw data reading, calibration, geometric correction, projection, cropping and parameter calculation.

The method of calibration is establishing the mathematical relationship between the real radiance and the value of the pixel, which can be written by:

$$Ra = G * P + C \tag{1}$$

where Ra is the real radiance corresponding to the pixel, P is the value of the pixel, G is the gain for count-radiance conversion equation and C is the constant for count-radiance conversion equation which can obtain from the header blocks in DAT files [29].

The method of geometric correction used in this study was Geographic Lookup Table (GLT). This method needs to establish the mathematical relationship between the longitude, latitude and the value of the pixel. The GLT method completes the geometric correction by finding the latitude and longitude corresponding to the pixel. Additionally, the method of projection used in this study was Mercator.

This study calculated the solar zenith angle (θ_0), sensor zenith angle (θ) and solar and sensor relative azimuth angles (ϕ) of internal waves at 10 min intervals. The expressions of these angles are [30,31]:

$$\theta_0 = arccos(cosLatcos\delta cosw + sinLat\ sin\delta) \tag{2}$$

where Lat is the latitude of the pixel. δ is the solar declination, which can be calculated by N (the accumulated days arranged in the order of the number of days, which can be obtained from DAT file [29]): $\delta = 0.006918 - 0.399912\cos\left(2\pi * \frac{N}{365}\right) + 0.010257\sin\left(2\pi * \frac{N}{365}\right) - 0.006758\cos 2\left(2\pi * \frac{N}{365}\right) + 0.000907\ \sin 2\left(2\pi * \frac{N}{365}\right)$. w is the solar hour angle, which also can be calculated by N:$w = 0.0172 - 0.4281\cos\left(2\pi * \frac{N}{365}\right) - 7.3515\sin\left(2\pi * \frac{N}{365}\right) - 3.4295cos2\left(2\pi * \frac{N}{365}\right) - 9.3619sin2\left(2\pi * \frac{N}{365}\right)$.

$$\theta = arcsin\left(\frac{R\ sin\gamma}{D}\right) \tag{3}$$

where R and D are the distances from the Earth center to the sensor and from the sensor to the pixel, they can be which can be obtained from DAT file [29]. γ is the intermediate variable and can be obtained by the latitude and longitude of the pixel and the longitude of the sensor: $\gamma = \arccos(cosLat\ cos(SatLon - Lon))$. $SatLon$ is the longitude of the sensor, Lon is the longitude of the pixel

$$\phi = \begin{cases} \beta_1 - \phi_1, & Lon - SatLon \le 0,\ Lat - SatLat < 0 \\ 180 - \beta_1 - \phi_1, & Lon - SatLon < 0,\ Lat - SatLat \ge 0 \\ 180 + \beta_1 - \phi_1, & Lon - SatLon \ge 0,\ Lat - SatLat > 0 \\ 360 - \beta_1 - \phi_1, & Lon - SatLon > 0,\ Lat - SatLat < 0 \end{cases} \tag{4}$$

where β_1 is the intermediate variable and can be calculated by: $cos\beta_1 = cot\gamma tanLat$. Lat and Lon are the latitude and longitude, respectively, of the pixel, $SatLat$ and $SatLon$ are the latitude and longitude, respectively, of the sensor, and ϕ_1 is the solar azimuth angle, which is expressed as:

$$\phi_1 = \arccos\left(\frac{\cos Lat\ sin\delta + sinLat\cos\delta\cos w}{cos(90 - \theta_0)}\right) \tag{5}$$

3. Method

In optical remote sensing, internal waves mainly appear in sunglint images. Therefore, it is very important to understand the physical imaging process of sunglint images, and the normalized sunglint radiance theory can describe this process.

3.1. Normalized Sunglint Radiance theory

The brightness of a given pixel in an optical remote sensing image is related to the solar radiance entering the sensor. When the sea surface is specular or nearly specular to reflect sunlight, most of the solar radiance is captured by the sensor, and the pixel corresponding to the sea surface is very bright. Conversely, the pixel corresponding to the sea surface is very dark.

The probability density function (pdf) of the wave slope determining sunglint reflection can be approximated by a Gaussian function and is given by [10]:

$$p\left(\theta,\theta_0,\phi,\sigma^2\right)=\frac{1}{2\pi\sigma_{up}\sigma_{cr}}\exp\left(-\frac{1}{2}\left(\frac{Z_{up}^2}{\sigma_{up}^2}+\frac{Z_{cr}^2}{\sigma_{cr}^2}\right)\right) \tag{6}$$

where Z_{up} and Z_{cr} denote the slope of the facet along the upwind and crosswind directions, respectively, and σ_{up}^2 and σ_{cr}^2 denote the sea surface roughness variance along these two directions.

The sea surface roughness variance is a linear function of the wind speed (W) based on an empirical model and is determined as [10]:

$$\sigma^2=0.003+0.00512W \tag{7}$$

Assuming the pdf is symmetric, Equation (6) can be simplified as [10]:

$$p\left(\theta,\theta_0,\phi,\sigma^2\right)=\frac{1}{2\pi\sigma^2}\exp\left(-\frac{1}{2}\left(\frac{Z_x^2+Z_y^2}{\sigma^2}\right)\right) \tag{8}$$

$$Z_x^2=\left(-\frac{sin\theta_0+sin\theta cos\phi}{cos\theta+cos\theta_0}\right)^2 \tag{9}$$

$$Z_y^2=\left(-\frac{sin\theta sin\phi}{cos\theta+cos\theta_0}\right)^2 \tag{10}$$

where Z_x^2 and Z_y^2 are the slopes of the facet along the x- and y-axis directions, respectively.

The relationship between the surface tilt (β) of a facet on the sea surface and Z_x^2 and Z_y^2 is [10]:

$$tan^2\beta=Z_x^2+Z_y^2 \tag{11}$$

Thus, the relationship between the surface tilt (β) and viewing geometry $\left(\theta,\theta_0,\phi,\sigma^2\right)$ is [10]:

$$tan^2\beta=\frac{sin^2\theta_0+sin^2\theta+2sin\theta_0 sin\theta cos\phi}{(cos\theta+cos\theta_0)^2} \tag{12}$$

Equation (8) can be simplified as [10]:

$$p\left(\theta,\theta_0,\phi,\sigma^2\right)=\frac{1}{2\pi\sigma^2}\exp\left(-\frac{1}{2}\left(\frac{tan^2\beta}{\sigma^2}\right)\right) \tag{13}$$

The glint radiance received by the sensor when observing the sea surface at an angle θ (not larger than 80°) is given by [10]:

$$L_{sg}=\frac{L_0\rho(\omega)p\left(\theta,\theta_0,\phi,\sigma^2\right)}{4cos^2\beta cos\theta} \tag{14}$$

where L_0 is the incident solar radiance on the sea surface, ω denotes the local reflection angle considering specular reflection of sunlight into the sensor by a facet thus tilted, which is determined by the spherical law of cosines as [10]:

$$cos2\omega = cos\theta + cos\theta_0 + sin\theta_0 sin\theta cos\phi \tag{15}$$

$\rho(\omega)$ is the Fresnel reflection coefficient for an unpolarized source and is given by [10]:

$$\rho(\omega) = \frac{1}{2}\left(\frac{sin^2(\omega - r)}{sin^2(\omega + r)} + \frac{tan^2(\omega - r)}{tan^2(\omega + r)}\right) \tag{16}$$

where r denotes the angle of refraction for water and is expressed as [10]:

$$\sin r = (sin\omega)/1.34 \tag{17}$$

Therefore, the normalized sunglint radiance of the sea surface is given by [10]:

$$N\left(\theta, \theta_0, \phi, \sigma^2\right) = \frac{L_0}{L_{sg}} = \frac{\rho(\omega)}{4} p\left(\theta, \theta_0, \phi, \sigma^2\right) \frac{\left(1 + tan^2\beta\right)^2}{\cos\theta} \tag{18}$$

The larger the normalized sunglint radiance (N_n) value of the pixel, the brighter the pixel is in the remote sensing image. Conversely, the smaller the normalized sunglint radiance (N_n) value of the pixel, the darker the pixel appears in the remote sensing image. Therefore, the normalized sunglint radiance (N_n) of the sea surface can be considered to explain the bright and dark features of internal waves in remote sensing images.

3.2. Critical Viewing Angle

There are three factors that influence the bright and dark features of internal waves in optical images, i.e., the sensor zenith angle (θ), solar zenith angle (θ_0) and relative azimuth angle (ϕ) based on the normalized sunglint radiance theory. Jackson pointed out the role of the critical sensor viewing angle in the brightness reversal process of internal waves in sunglint images [15].

Figure 3 shows the critical sensor viewing angle (θ_c). As shown in Figure 3, the curves of the normalized sunglint radiance (N_n) change with the multi-sensor zenith angle (θ) when both the solar zenith angle (θ_0) and relative azimuth angle (ϕ) are fixed, and these curves intersect to generate two intersection points. Choosing the left intersection point as an example, based on the occurrence of the sensor zenith angle (θ) of the internal wave on the left side of the intersection point, the sea surface is darker than the convergence zone of the internal wave because the roughness variance of the sea surface is lower than that in the convergence zone of the internal wave. In addition, the sea surface is brighter than the divergence zone of the internal wave because the roughness variance of the sea surface is higher than that in the convergence zone of the internal wave. However, based on the occurrence of the sensor zenith angle (θ) of the internal wave on the right side of the intersection point, the sea surface is brighter than the convergence zone of the internal wave because the roughness variance of the sea surface is lower than that in the convergence zone of the internal wave, and the sea surface is darker than the divergence zone of the internal wave because the roughness variance of the sea surface is higher than that in the convergence zone of the internal wave. Therefore, in regard to the sensor zenith angle (θ) of internal waves on the left and right sides of the intersection point, the bright and dark features of internal waves reveal opposite patterns, which can explain why the bright and dark features of internal waves at different locations in a remote sensing image vary. The above intersection points are denoted as the critical sensor viewing angle (θ_c) [15].

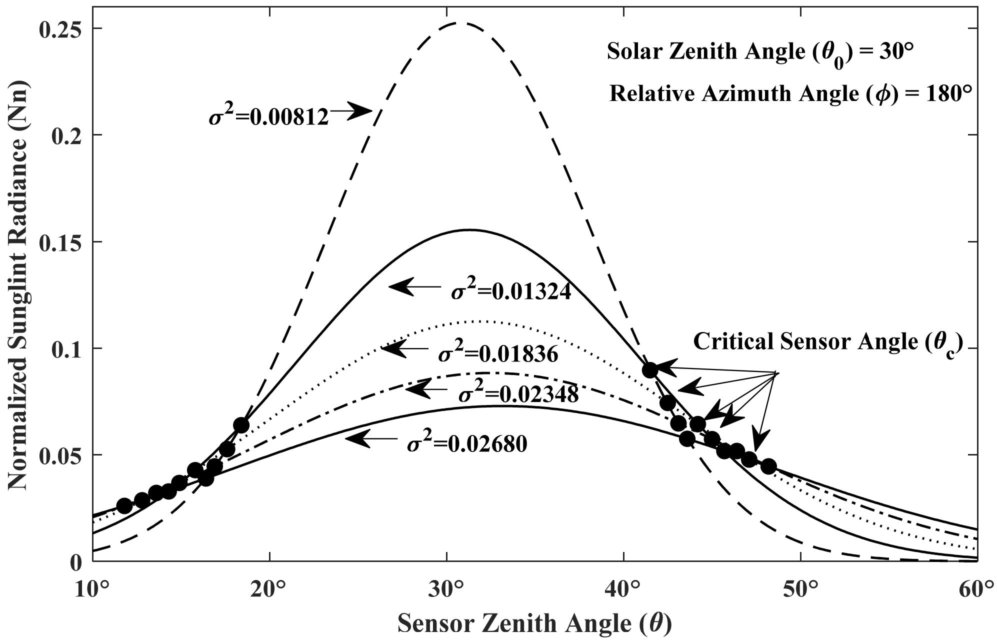

Figure 3. Schematic diagram showing the critical sensor viewing angle (θ_c). The solar zenith angle (θ_0) is 30°, and the relative azimuth angle (ϕ) is 180°, which remain fixed. The sea surface roughness variance (σ^2) corresponding to the curves is 0.00812, 0.01324, 0.001836, 0.02348 and 0.02680.

The sensor viewing angle can explain the phenomenon that the bright and dark features of internal waves at various locations in a remote sensing image differ. In contrast, the sensor viewing angle cannot explain the phenomenon whereby the bright and dark features of internal waves in various temporal images are also different.

According to the normalized sunglint radiance theory, the solar zenith angle (θ_0), sensor zenith angle (θ) and relative azimuth angle (ϕ) are the main factors that determine the brightness of internal waves in remote sensing images. A plot of the normalized sunglint radiance (N_n) changes with the sensor zenith angle (θ) in accordance with a Gaussian distribution, and a plot of the normalized sunglint radiance (N_n) changes with the solar zenith angle (θ_0) in accordance with a Gaussian distribution, indicating the probable occurrence of the critical solar viewing angle. This paper verifies the occurrence of the critical solar viewing angle based on the normalized sunglint radiance (N_n) and critical sensor viewing angle theories.

Figure 4 shows curves of the change in the normalized sunglint radiance (N_n) at multiple solar zenith angles (θ_0) when the sensor zenith angle (θ) and relative azimuth angle (ϕ) remain fixed. The curves intersect, and each pair of curves produces two intersections. Based on the occurrence of the solar zenith angle (θ_0) of the internal wave on the left side of the intersection point, the sea surface is darker than the convergence zone of the internal wave because the roughness variance of the sea surface is lower than that in the convergence zone of the internal wave, and the sea surface is brighter than the divergence zone of the internal wave because the roughness variance of the sea surface is higher than that in the convergence zone of the internal wave. However, based on the occurrence of the solar zenith angle (θ_0) of the internal wave on the right side of the intersection point, the sea surface is brighter than the convergence zone of the internal wave because the roughness variance of the sea surface is lower than that in the convergence zone of the internal wave, and the sea surface is darker than the divergence zone of the internal wave because the roughness variance of the sea surface is higher than that in the convergence zone of the internal wave. When the solar zenith angle (θ_0) of internal waves is located on the left and right sides of the intersection point, the bright and dark features, respectively, are the opposite, which can be denoted as the critical solar viewing angle (θ_{0c}).

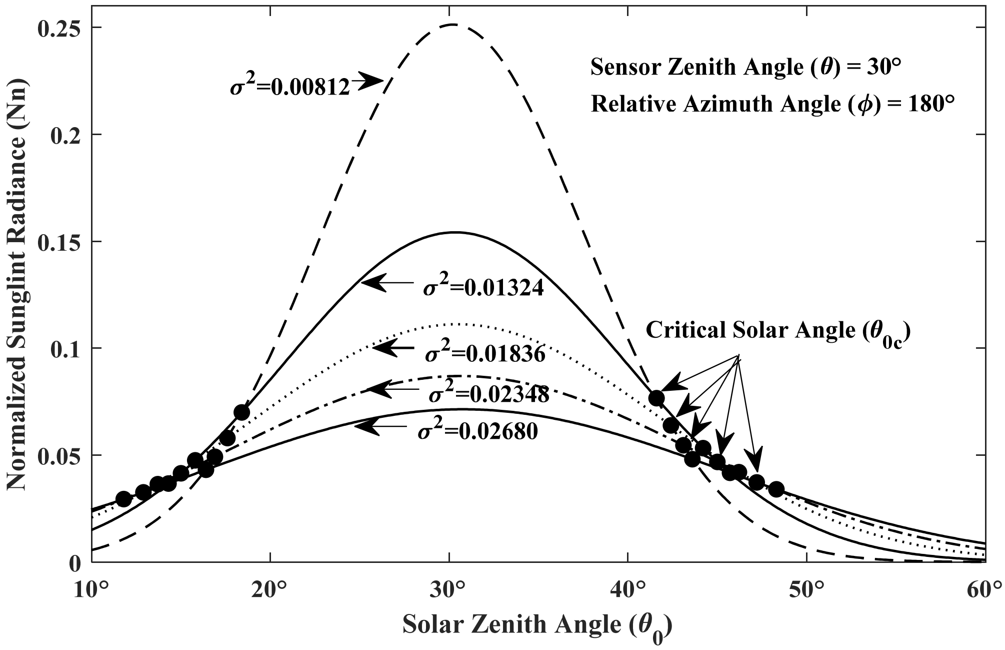

Figure 4. Schematic diagram showing the critical solar viewing angle (θ_{0c}). The sensor zenith angle (θ) is 30°, and the relative azimuth angle (ϕ) is 180°, which remain fixed. The sea surface roughness variance (σ^2) corresponding to the curves is 0.00812, 0.01324, 0.001836, 0.02348 and 0.02680.

4. Results

4.1. Brightness Reversal of Internal Waves in Himawari-8 Images

There occurs an ISW packet with four solitons in every Himawari-8 image of the Celebes Sea acquired on 21 September 2020 from 04:50–05:40 UTC, as shown in Figure 5. As shown in the six images of the Celebes Sea, the ISW packet is framed by a red box, and the red solid line corresponds to the profile of the crest of the ISW on the upper right side. Since we applied an image spatial resolution of 500 m in this paper, the bright and dark features are difficult to clearly observe when both the wavelength and amplitude are small. Hence, we only examine the bright–dark patterns of the leading wave of the wave packet in this paper. According to the profile of the crest of the leading wave, as shown in Figure 5a, the leading wave reveals dark–bright patterns where the dark band is not obvious, probably because the sea background is also very dark. The leading wave shows bright to dark–bright patterns in Figure 5b–e, which has never been reported in previous studies. Subsequently, the leading wave shows dark-bright patterns in Figure 5f, which is also observed in Figure 5a. This phenomenon suggests that a brightness reversal process occurs during ISWs propagation, which transitions from a dark-bright pattern through a unique process involving a bright–dark–bright pattern and then returns to the dark–bright pattern.

Figure 5 shows the brightness reversal of the ISW packet in the Celebes Sea at 21 September 2020 04:50–05:40 UTC. In order to avoid the influence of the descending internal wave or the ascending internal wave on brightness reversal and some another misjudgment, the time sequence changes of the radiances of certain points on the same leading wave with time and space was discussed in Figure 6. Five points in different positions on the same leading wave at 04:50–05:40 UTC are used to discussed to enhance the reliability of the result.

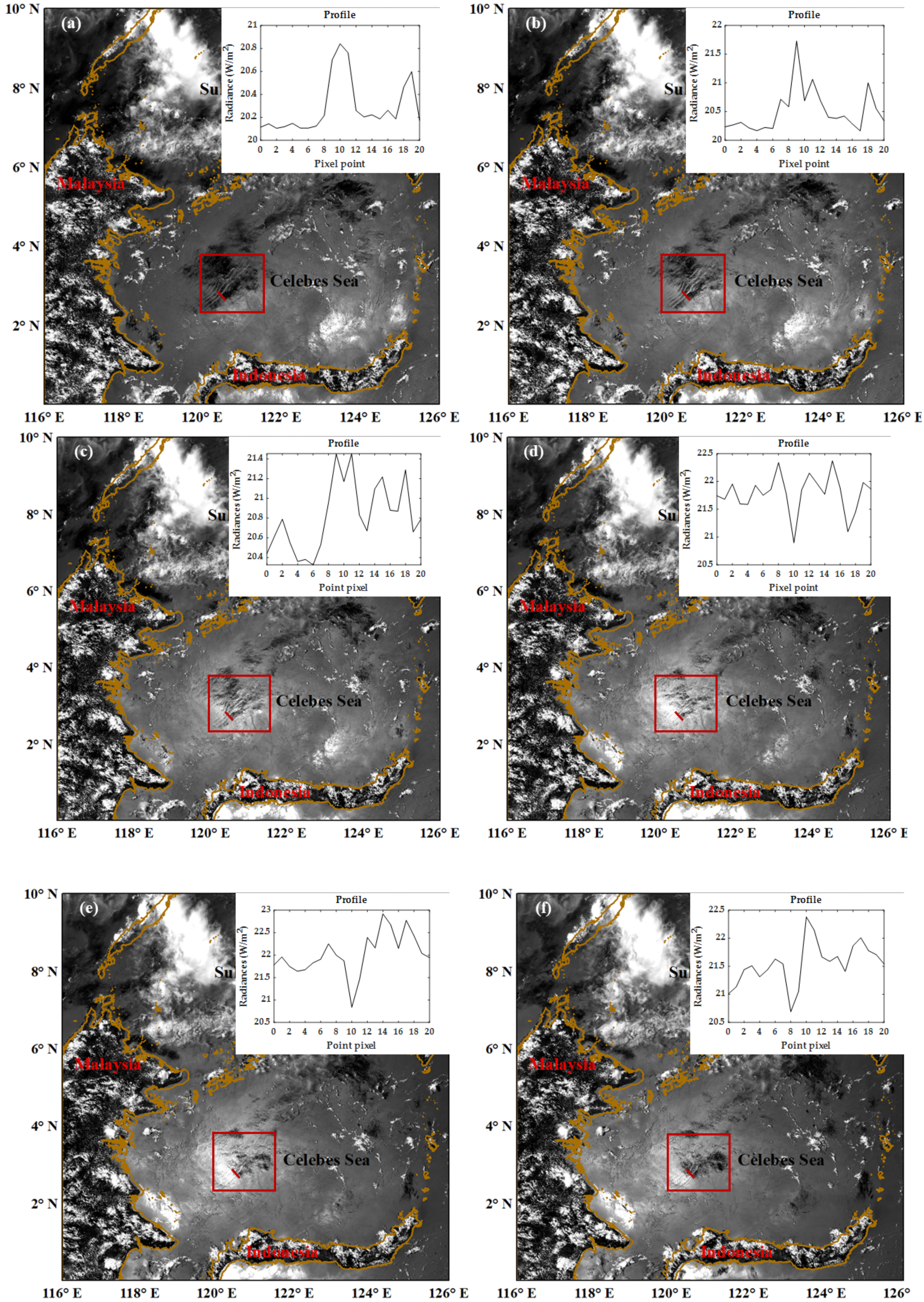

Figure 5. Himawari-8 images of the Celebes Sea acquired on 21 September 2020. The internal solitary wave packet is framed by a red box, and the red solid line corresponds to the profile of the crest of the leading wave in the upper part of the right side. (**a**–**f**) show images with an interval of 10 min between 04:50 UTC and 05:40 UTC.

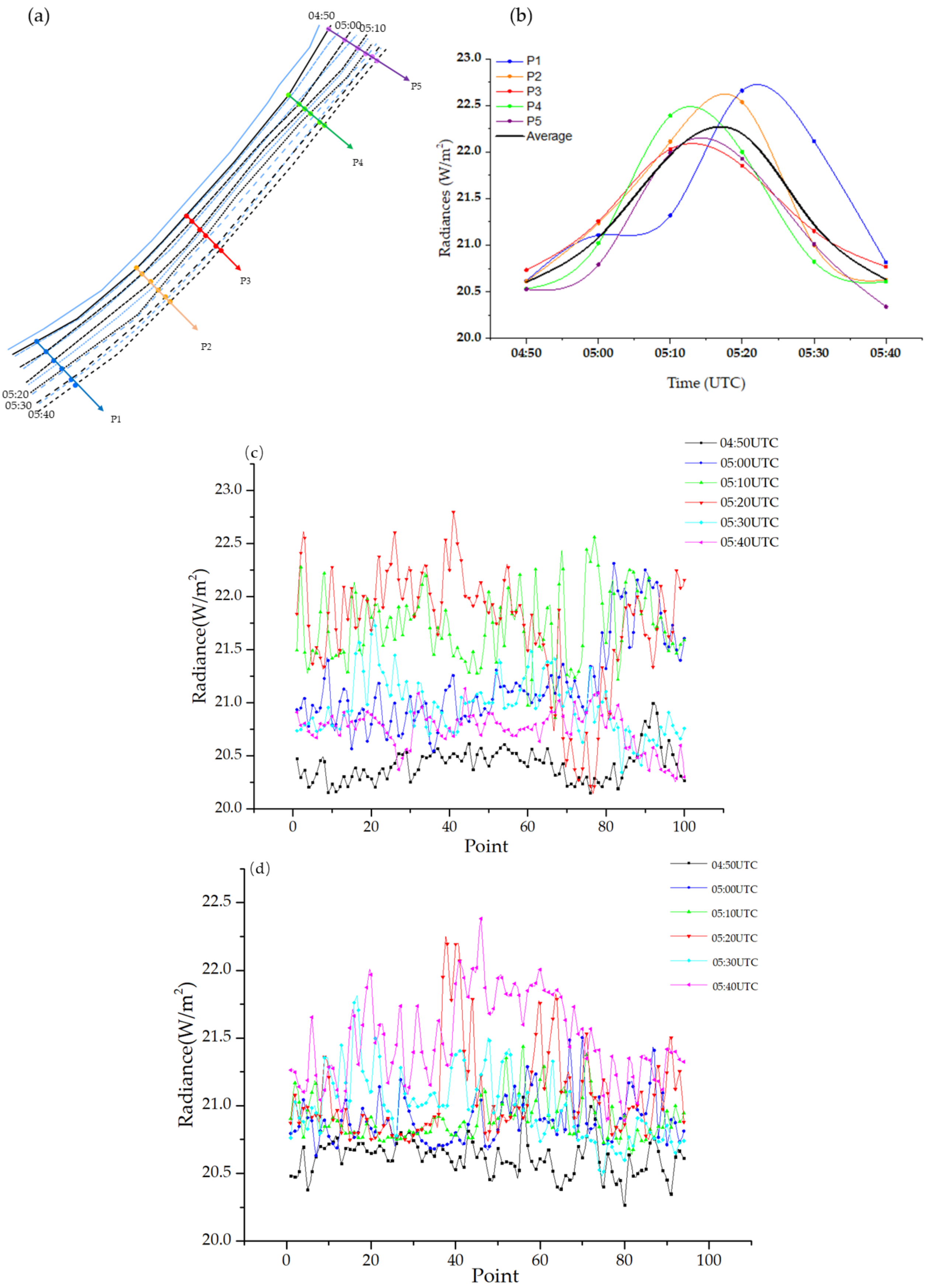

Figure 6. *Cont*.

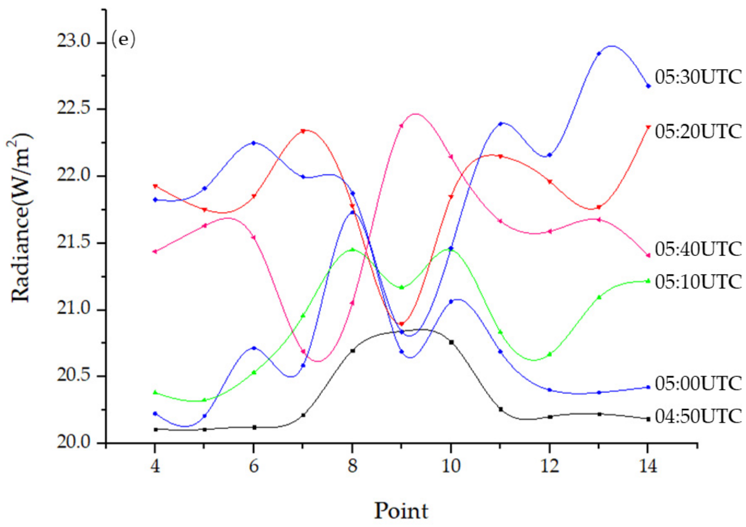

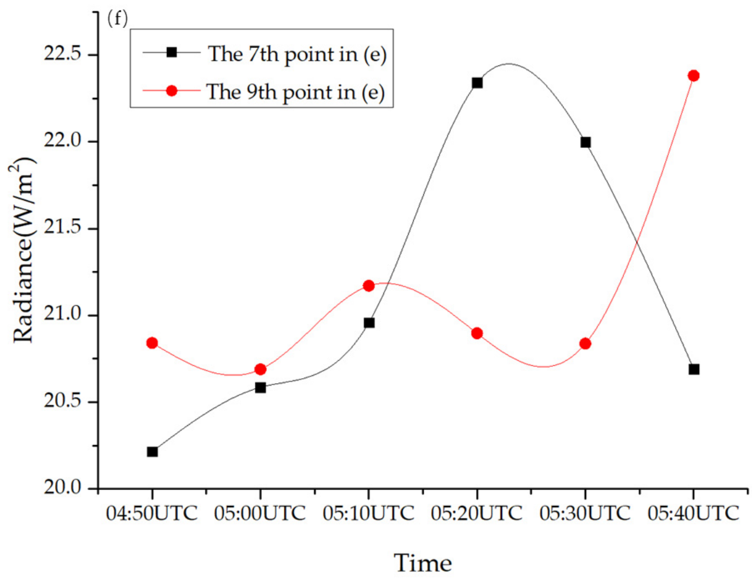

Figure 6. The time sequence change of the radiance of 5 certain points on the same leading wave with time and space. (**a**) shows the spatial changes of 5 points on the same leading wave at 04:50–05:40 UTC, and the types of the same leading wave at different moments are different, and the 5 points are represented by different colors, which the arrows show the propagation direction; (**b**) shows the time changes of the radiances of 5 certain points on the leading wave. The colors of 5 points in (**a**) correspond to the colors of 5 curves in (**b**) and the average of 5 curves is also shown. (**c**) shows the radiance curves of the dark band at 04:50-05:40 UTC. The radiances at 04:50 UTC are lower than 05:00 UTC as a whole. Additionally, the radiances at 05:00 UTC are lower than 05:10 UTC as a whole. The radiances at 05:10 UTC are lower than 05:20 UTC as a whole. Therefore, the radiance of dark band is increasing. The radiances at 05:40 UTC are lower than 05:30 UTC, so the radiance of the dark band is decreasing. (**d**) shows the radiances of the bright band at 04:50–05:40 UTC. The radiances at 04:50 UTC are lower than 05:00 UTC as a whole. Additionally, the radiances at 05:00 UTC are lower than 05:10 UTC as a whole. The radiances at 05:10 UTC are lower than 05:20 UTC as a whole. The radiances at 05:20 UTC are lower than 05:30 UTC as a whole. The radiances at 05:30 UTC are lower than 05:40 UTC as a whole. Therefore, the radiance of the bright band is increasing. (**e**) superimposes the profiles of internal waves in Figure 5 at 04:50–05:40 UTC. The bright and dark band in images at 04:50–05:40 UTC are corresponding. The X-axis number is corresponding to the X-axis number of profiles in Figure 5. (**f**) shows the radiance curves of the 7th point and the 9th point in Figure 6e at different moments.

In Figure 6a, the spatial changes of five points on the same leading wave at 04:50–05:40 UTC are shown. Due to the low spatial resolution of Himawari-8 images, the leading wave does not seem to be very smooth and the distances of internal wave at different moments are not equal everywhere. The five points in the leading wave at 04:50 UTC are randomly selected in order to reduce errors. The position of five points in the leading wave at 05:00–05:40 UTC is determined by the propagation direction and the speed of the leading wave. It should be noted that the speed of internal waves is about 2 m/s, which referenced to the work of predecessors on the study of internal waves in the Celebes Sea [24].

Figure 6b is the time changes of radiances of five certain points in six black curves in Figure 6a. The colors of the five points in Figure 6a correspond to the colors of curves in Figure 6b. In order to showing the characteristics of the five curves more intuitively, the black curve is also shown in Figure 6b, which is the average of the five curves. The six curves all appear as a "rising–falling" trend or parabolic form, which illustrated the authenticity of the brightness reversal of the internal wave in Figure 5.

Figure 6c shows the radiance curves of dark band in Figure 6a (note that dark band mentioned here is the dark band in Figure 6a, because of the brightness reverse, it may be a bright band or a dark band in Figure 5b–f at different moments. Due to the low spatial resolution of the images, the curves are not smooth, but the trend of curves are clear from 04:50–05:20 UTC. From 04:50–05:20 UTC, the radiance of dark band is increasing, and from 05:30–05:40 UTC, the radiance of dark band is decreasing, so the dark band turns to bright band and into dark band. This phenomenon is exactly the same as the trend of the curve in Figure 6b. From the 60th point to the 80th point of the radiances curve at 05:20 UTC, the radiances are abnormally low. The reason for this phenomenon is that the solar, the sea surface and the sensor constitute a specular reflection condition at 05:20 UTC, and the wind increases sea surface roughness resulting in abnormally low radiances. Additionally, the influence of wind is also clearly visible in Figure 5d.

Figure 6d shows the radiance curves of bright band in Figure 6a (note that bright band mentioned here is the bright band in Figure 6a, because of the brightness reverse, it may be a bright band or a dark band in Figure 5b–f at different moments). From 04:50–05:40 UTC, the radiance of the bright band is always increasing, instead of first decreasing and then increasing. However, the bright band first turns to a dark band and then into a bright band. The reason for this phenomenon is that the sensor, the solar, and the internal waves have become a special geometric condition (the sensor zenith angle is equal to the solar zenith angle) at 05:20 UTC, and most sunlight enters the sensor. Additionally, the bigger the difference between the sensor zenith angle and the solar zenith angle the bigger, the less light enters the sensor. Therefore, the many radiances of bright band in Figure 5a are lower than Figure 5b–d, which can explain that the radiance of bright band at 04:50 UTC are lower than 05:00–05:30 UTC.

What needs to be explained is that Figure 6c is the radiance curves of six black lines in Figure 6a,d is the radiance curves of six light blue lines in Figure 6a.

Figure 6e,f again verify this result. Figure 6e superimposes the profiles of internal waves in Figure 5 at 04:50–05:40 UTC. Figure 6f shows the radiance curves of the seventh point and the ninth point in Figure 6e at different moments. The radiances curve of the seventh point is first increasing and then decreasing, which is same as the radiances of the dark band in Figure 6c. The radiances curve of the ninth point is first increasing and then decreasing, which is same as the radiances of the bright band in Figure 6d.

4.2. The Changes of Angles of the Leading Wave

Figure 5 shows an obvious brightness reversal phenomenon. According to the normalized sunglint radiance theory, the bright and dark features of the leading wave in the remote sensing image are affected by the three angles of the solar zenith angle (θ_0), sensor zenith angle (θ), and relative azimuth angle (ϕ) of the leading wave.

Figure 7a shows a part of the Himawari-8 image of the Celebes Sea acquired on 21 September 2020 at 04:50 UTC, and the ISW packet is located on the left side of the image. The bright and dark features of the leading wave are shown in Figure 5a. The small white patches in the image are clouds in the atmosphere, and the white solid line is the scan line of the AHI sensor onboard the Himawari-8 satellite.

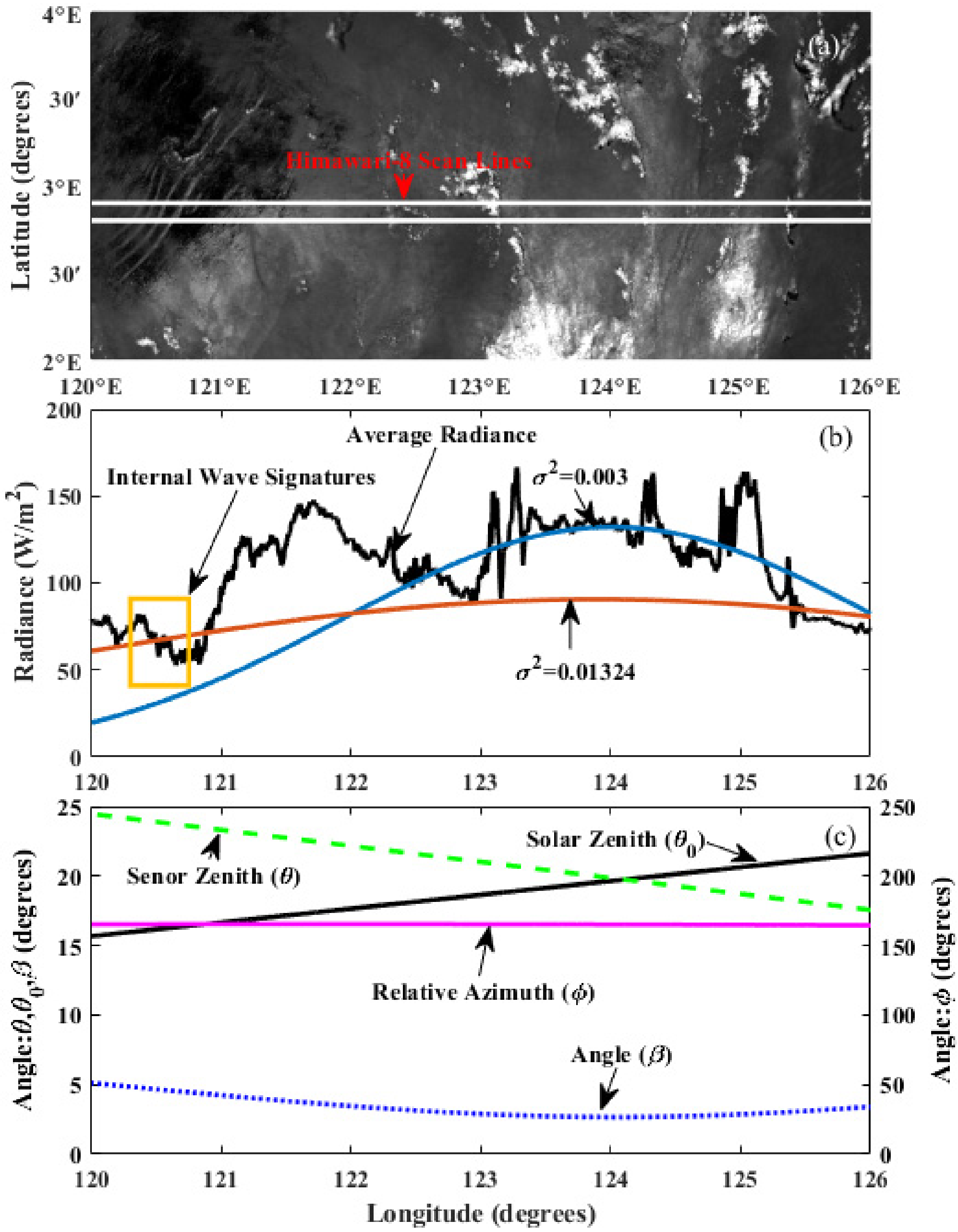

Figure 7. Analysis of the image acquired on 21 September 2020 at 04:50 UTC. (**a**) shows part of the Himawari-8 image of the Celebes Sea acquired on 21 September 2020 at 04:50 UTC, and the white solid line indicates the scan line of the AHI sensor onboard the Himawari-8 satellite; (**b**) shows curves of the normalized solar radiance calculated with roughness variance (σ^2) values of 0.003 and 0.01324 and the average measured radiance along the scan line, and the yellow box marks the position of the internal solitary waves. The blue and orange curves indicate the radiance information of the sea surface background and internal solitary waves, respectively; (**c**) shows the changes in the solar zenith angle (θ_0), sensor zenith angle (θ), relative azimuth angle (ϕ), and surface facet tilt (β) along the AHI sensor scan line. The solid black line indicates the change in the solar zenith angle (θ_0) along the scan line. The green dashed line indicates the change in the sensor zenith angle (θ) along the scan line. The purple solid line indicates the relative azimuth angle (ϕ) along the scan line. The blue dotted line indicates the change in the surface facet tilt (β) along the scan line.

Figure 7b shows curves of the normalized solar radiance calculated with roughness variance (σ^2) values of 0.003 and 0.01324 and the average measured radiance along the scan line. To reduce the errors caused by cloud cover and other factors, the measured radiance is the average value of 40 adjacent scan lines, which presents an approximate Gaussian distribution as a whole. The yellow box in Figure 7b marks the ISW position, the blue curve fits the radiance information of the sea surface background well, and the orange curve fits the radiance information of the ISWs, which was verified by Jackson et al. [15].

Figure 7c shows the changes in the solar zenith angle (θ_0), sensor zenith angle (θ), relative azimuth angle (ϕ) and surface facet tilt (β) along the AHI sensor scan line. With increasing longitude, the sensor zenith angle (θ) gradually decreases. This occurs because the Himawari-8 satellite center exhibits a longitude of 140.7°E, which is located on the right side of the study area. With increasing longitude, the solar zenith angle (θ_0) gradually increases. This occurs because solar radiation ensues on the left side of the study area. The change in the sensor zenith angle (θ) and solar zenith angle (θ_0) is exactly the opposite. The relative azimuth angle (ϕ) gradually decreases, but the change is small. The surface facet tilt (β) first decreases and then increases, and its minimum value occurs along the central axis of the sunglint in the image. The solar zenith angle (θ_0), sensor zenith angle (θ), relative azimuth angle (ϕ), and surface facet tilt (β) of the leading wave are approximately 16.19°, 23.70°, 165.40°, and 4.61°, respectively.

Figure 8a shows part of the Himawari-8 image of the Celebes Sea acquired on 21 September 2020 at 05:00 UTC, which is the image at the next moment depicted in Figure 7a. Similar to Figure 7a, the ISW packet is located on the left side of the image, and the bright and dark features of the leading wave are shown in detail in Figure 5b. The small white patches indicate clouds in the atmosphere, and the solid white line represents the scan line of the AHI sensor onboard the Himawari-8 satellite.

Figure 8b shows curves of the normalized solar radiance calculated with roughness variance (σ^2) values of 0.003 and 0.01324 and the average measured radiance along the scan line. The measured radiance is the average value of 40 adjacent scan lines, which exhibits an approximate Gaussian distribution as a whole. The yellow box in Figure 8b marks the position of ISWs, the blue curve suitably fits the radiance information of the sea surface background, and the orange curve fits the ISW radiance information.

Figure 8c shows the changes in the solar zenith angle (θ_0), sensor zenith angle (θ), relative azimuth angle (ϕ), and surface facet tilt (β) along the AHI sensor scan line. At this time, the solar zenith angle (θ_0), sensor zenith angle (θ), relative azimuth angle (ϕ), and surface facet tilt (β) of the leading wave are approximately 18.67°, 23.74°, 166.43°, and 3.64°, respectively.

Figure 9a shows the Himawari-8 image of the Celebes Sea acquired on 21 September 2020 at 05:10 UTC, which is the image at the next moment depicted in Figure 8a. The ISW packet is located at the center of the image, and the bright and dark features of the leading wave are shown in detail in Figure 5c. The small white patches indicate clouds in the atmosphere, and the solid white line is the scan line of the AHI sensor onboard the Himawari-8 satellite.

Figure 9b shows curves of the normalized solar radiance calculated with roughness variance (σ^2) values of 0.003 and 0.01324 and the average measured radiance along the scan line. The measured radiance is the average value of 40 adjacent scan lines, which exhibits an approximate Gaussian distribution as a whole. The yellow box in Figure 9b marks the position of the ISWs, the blue curve fits the radiance information of the sea surface background well, while the orange curve fits the radiance information of the ISWs.

Figure 9c shows the changes of solar zenith angle (θ_0), sensor zenith angle (θ), relative azimuth angle (ϕ) and surface facet tilt (β) on AHI sensor scan line. At this time, the solar zenith angle (θ_0), sensor zenith angle (θ), relative azimuth angle (ϕ), and surface facet tilt (β) of the leading wave are approximately 21.50°, 23.78°, 167.23°, and 2.90°, respectively.

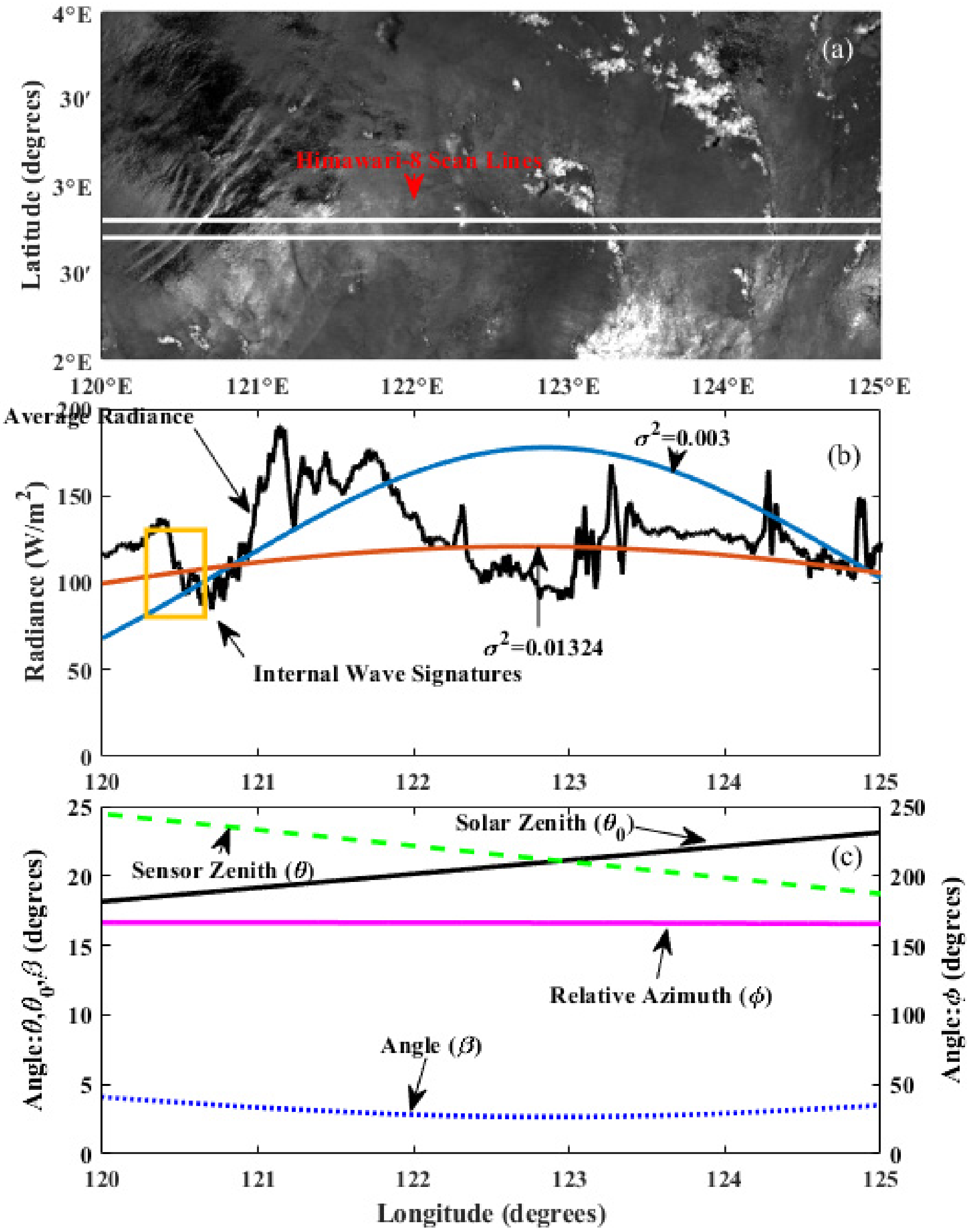

Figure 8. Analysis of the image acquired on 21 September 2020 at 05:00 UTC. (**a**) shows part of the Himawari-8 image of the Celebes Sea acquired on 21 September 2020 at 05:00 UTC, and the white solid line indicates the scan line of the AHI sensor onboard the Himawari-8 satellite; (**b**) shows curves of the normalized solar radiance calculated with roughness variance (σ^2) values of 0.003 and 0.01324 and the average measured radiance along the scan line, and the yellow box marks the position of the internal solitary waves. The blue and orange curves represent the radiance information of the sea surface background and internal solitary waves, respectively; (**c**) shows the changes in the solar zenith angle (θ_0), sensor zenith angle (θ), relative azimuth angle (ϕ), and surface facet tilt (β) along the AHI sensor scan line. The solid black line represents the change in the solar zenith angle (θ_0) along the scan line. The green dashed line represents the change in the sensor zenith angle (θ) along the scan line. The purple solid line represents the relative azimuth angle (ϕ) along the scan line. The blue dotted line represents the change in the surface facet tilt (β) along the scan line.

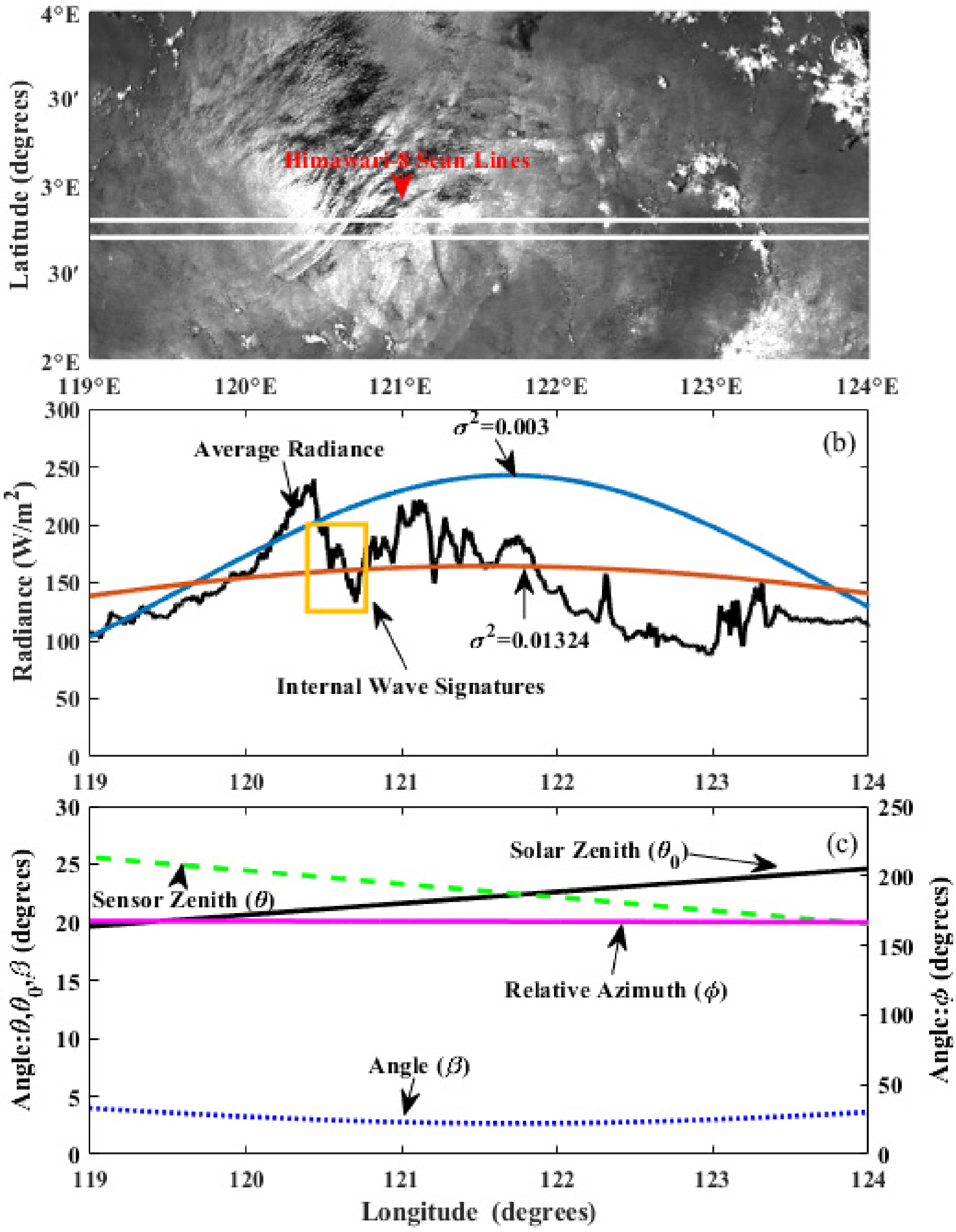

Figure 9. Analysis of the image acquired on 21 September 2020 at 05:10 UTC. (**a**) shows part of the Himawari-8 image of the Celebes Sea acquired on 21 September 2020 at 05:10 UTC, and the white solid line is the scan line of the AHI sensor onboard the Himawari-8 satellite; (**b**) shows curves of the normalized solar radiance calculated with roughness variance (σ^2) values of 0.003 and 0.01324 and the average measured radiance along the scan line, and the yellow box marks the position of the internal solitary waves. The blue and orange curves indicate the radiance information of the sea surface background and internal solitary waves, respectively; (**c**) shows the changes in the solar zenith angle (θ_0), sensor zenith angle (θ), relative azimuth angle (ϕ), and surface facet tilt (β) along the AHI sensor scan line. The solid black line indicates the change in the solar zenith angle (θ_0) along the scan line. The green dashed line indicates the change in the sensor zenith angle (θ) along the scan line. The purple solid line indicates the relative azimuth angle (ϕ) along the scan line. The blue dotted line indicates the change in surface facet tilt (β) along the scan line.

Figure 10a shows the Himawari-8 image of the Celebes Sea acquired on 21 September 2020 at 05:20 UTC, which is the image at the next moment depicted in Figure 9a. The

ISW packet is located at the center of the image, and the bright and dark features of the leading wave are shown in detail in Figure 5d. The small white patches are clouds in the atmosphere, and the solid white line is the scan line of the AHI sensor onboard the Himawari-8 satellite.

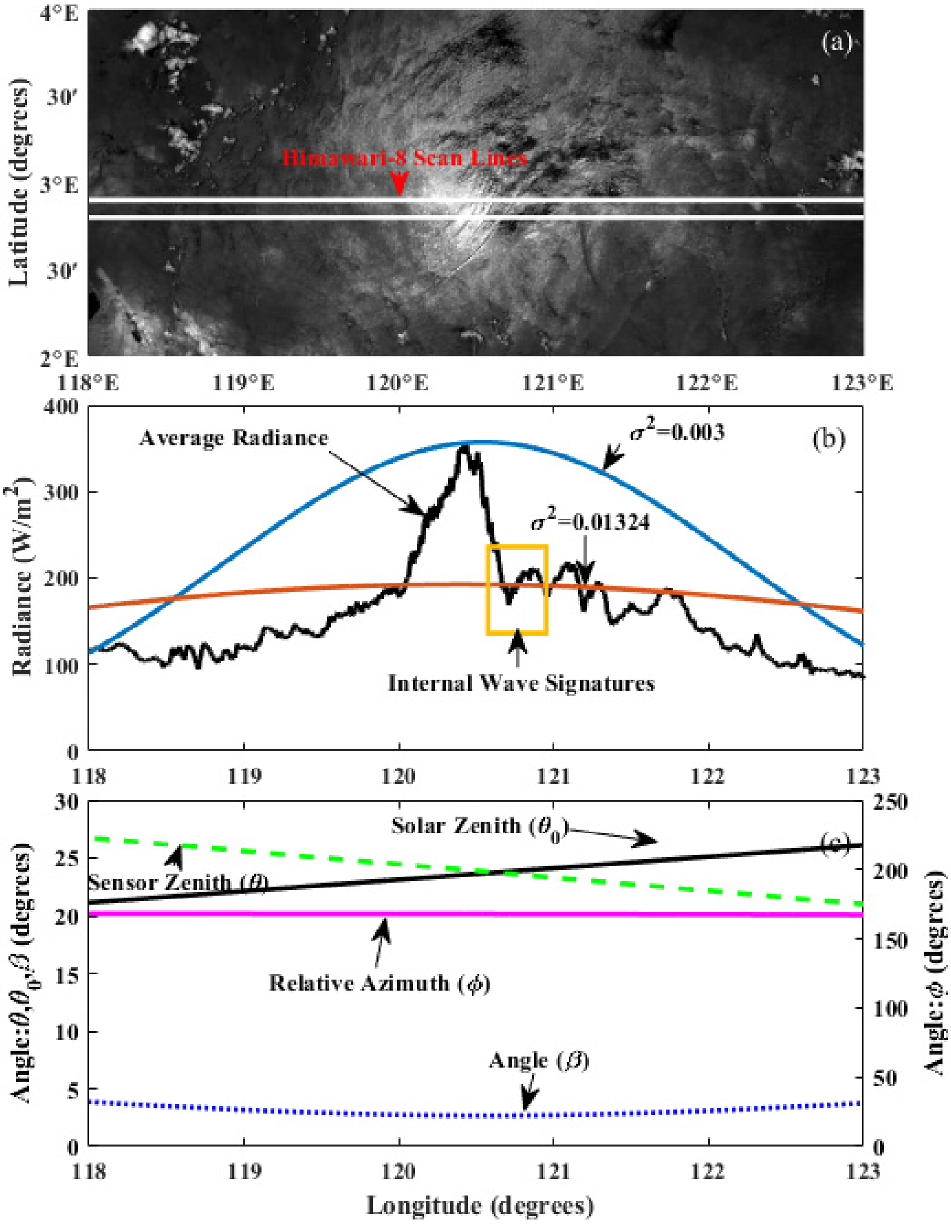

Figure 10. Analysis of the image acquired on 21 September 2020 at 05:20 UTC. (**a**) shows part of the Himawari-8 image of the Celebes Sea acquired on 21 September 2020 at 05:20 UTC, and the white solid line represents the scan line of the AHI sensor onboard the Himawari-8 satellite; (**b**) shows curves of the normalized solar radiance calculated with roughness variance (σ^2) values of 0.003 and 0.01324 and the average measured radiance along the scan line, and the yellow box marks the position of the internal solitary waves. The blue and orange curves represent the radiance information of the sea surface background and internal solitary waves, respectively; (**c**) shows the changes in the solar zenith angle (θ_0), sensor zenith angle (θ), relative azimuth angle (ϕ), and surface facet tilt (β) along the AHI sensor scan line. The solid black line represents the change in the solar zenith angle (θ_0) along the scan line. The green dashed line represents the change in the sensor zenith angle (θ) along the scan line. The purple solid line represents the relative azimuth angle (ϕ) along the scan line. The blue dotted line represents the change in surface facet tilt (β) along the scan line.

Figure 10b shows curves of the normalized solar radiance calculated with roughness variance (σ^2) values of 0.003 and 0.01324 and the average measured radiance along the scan line. The measured radiance is the average value based on 40 adjacent scan lines, which presents an approximate Gaussian distribution as a whole. The yellow box in Figure 10b marks the position of the ISWs, the blue curve suitably fits the radiance information of the sea surface background, while the orange curve fits the ISW radiance information.

Figure 10c shows the changes in the solar zenith angle (θ_0), sensor zenith angle (θ), relative azimuth angle (ϕ) and surface facet tilt (β) along the AHI sensor scan line. At this time, the solar zenith angle (θ_0), sensor zenith angle (θ), relative azimuth angle (ϕ) and surface facet tilt (β) of the leading wave are approximately 23.64°, 23.82°, 167.87°, and 2.67°, respectively. The ISW packet is almost located at the "specular reflection point" (the solar zenith angle (θ_0) is equal to the sensor zenith angle (θ)), which also explains why the ISW packet in Figure 5d is unusually brighter than the sea surface background.

Figure 11a shows the Himawari-8 image of the Celebes Sea acquired on 21 September 2020 at 05:30 UTC, which is the image at the next moment depicted in Figure 10a. The ISW packet is located on the right side of the image, and the bright and dark features of the leading wave are shown in detail in Figure 5e. The small white patches indicate clouds in the atmosphere, and the solid white line is the scan line of the AHI sensor onboard the Himawari-8 satellite.

Figure 11b shows curves of the normalized solar radiance calculated with roughness variance (σ^2) values of 0.003 and 0.01324 and the average measured radiance along the scan line. The measured radiance is the average value based on 40 adjacent scan lines, which reveals an approximate Gaussian distribution as a whole. The yellow box in Figure 11b marks the position of the ISWs, the blue curve fits the radiance information of the sea surface background well, while the orange curve fits the radiance information of the ISWs.

Figure 11c shows the changes in the solar zenith angle (θ_0), sensor zenith angle (θ), relative azimuth angle (ϕ), and surface facet tilt (β) along the AHI sensor scan line. At this time, the solar zenith angle (θ_0), sensor zenith angle (θ), relative azimuth angle (ϕ), and surface facet tilt (β) of the leading wave reach approximately 26.19°, 23.86°, 168.40°, and 2.99°, respectively.

Figure 12a shows the Himawari-8 image of the Celebes Sea acquired on 21 September 2020 at 05:40 UTC, which is the image at the next moment depicted in Figure 11a. The ISW packet is located on the right side of the image, and the bright and dark features of the leading wave are shown in detail in Figure 5f. The small white patches indicate clouds in the atmosphere, and the solid white line is the scan line of the AHI sensor onboard the Himawari-8 satellite.

Figure 12b shows curves of the normalized solar radiance calculated with roughness variance (σ^2) values of 0.003 and 0.01324 and the average measured radiance along the scan line. The measured radiance is the average value of 40 adjacent scan lines, which exhibits an approximate Gaussian distribution as a whole. The yellow box in Figure 12b marks the position of the ISWs, the blue curve fits the radiance information of the sea surface background well, and the orange curve fits the radiance information of the ISWs.

Figure 12c shows the changes in the solar zenith angle (θ_0), sensor zenith angle (θ), relative azimuth angle (ϕ), and surface facet tilt (β) on the AHI sensor scan line. At this time, the solar zenith angle (θ_0), sensor zenith angle (θ), relative azimuth angle (ϕ), and surface facet tilt (β) of the leading wave reach approximately 28.68°, 23.90°, 168.84°, and 3.72°, respectively.

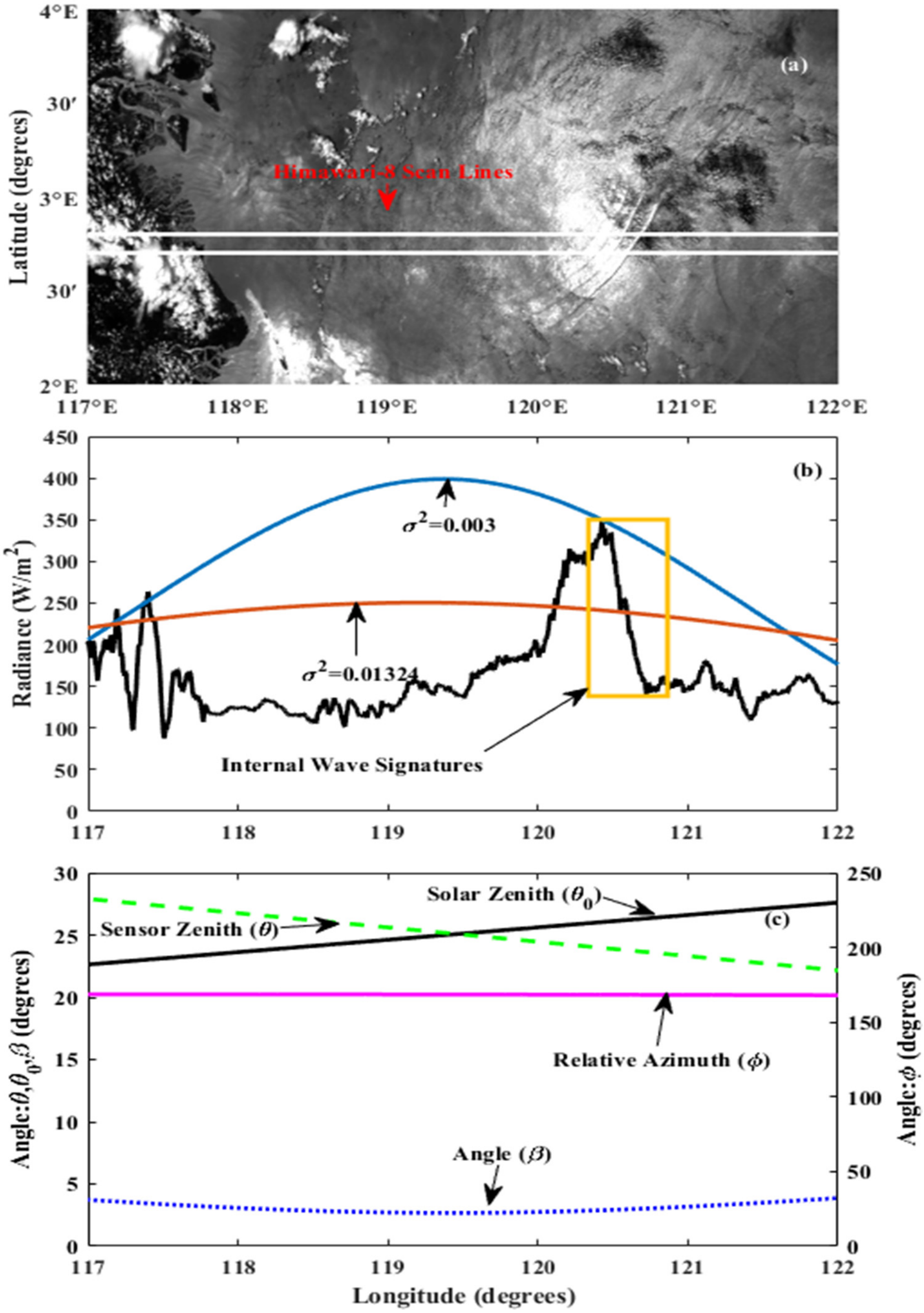

Figure 11. Analysis of the image acquired on 21 September 2020 at 05:30 UTC. (**a**) shows part of the Himawari-8 image of the Celebes Sea acquired on 21 September 2020 at 05:30 UTC, and the white solid line represents the scan line of the AHI sensor onboard the Himawari-8 satellite; (**b**) shows curves of the normalized solar radiance calculated with roughness variance (σ^2) values of 0.003 and 0.01324 and the average measured radiance along the scan line, and the yellow box marks the position of the internal solitary waves. The blue and orange curves indicate the radiance information of the sea surface background and internal solitary waves, respectively; (**c**) shows the changes in the solar zenith angle (θ_0), sensor zenith angle (θ), relative azimuth angle (ϕ), and surface facet tilt (β) along the AHI sensor scan line. The solid black line indicates the change in the solar zenith angle (θ_0) along the scan line. The green dashed line indicates the change in the sensor zenith angle (θ) along the scan line. The purple solid line indicates the relative azimuth angle (ϕ) along the scan line. The blue dotted line indicates the change in surface facet tilt (β) along the scan line.

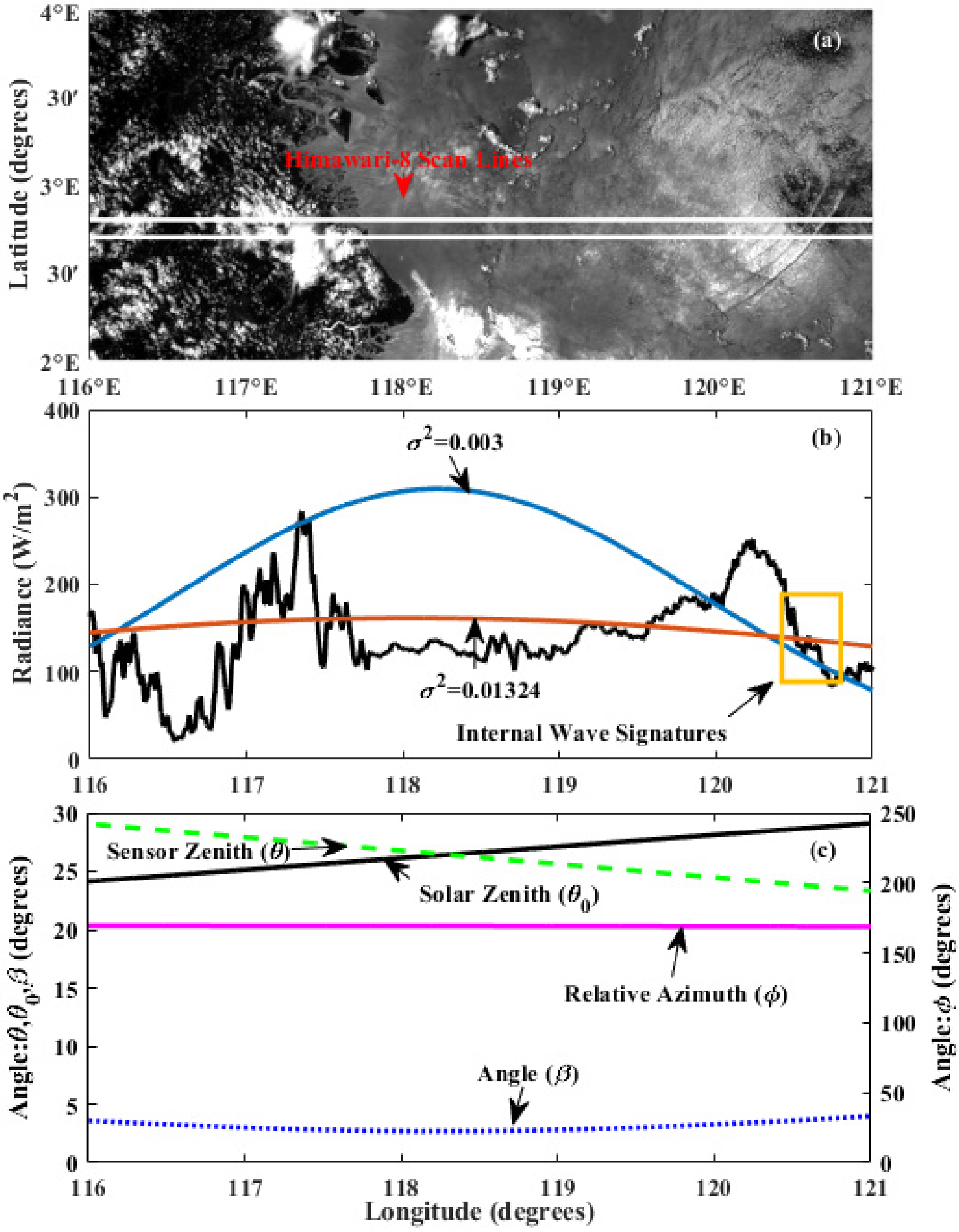

Figure 12. Analysis of the image acquired on 21 September 2020 at 05:40 UTC. (**a**) shows part of the Himawari-8 image of the Celebes Sea acquired on 21 September 2020 at 05:40 UTC, and the white solid line is the scan line of the AHI sensor onboard the Himawari-8 satellite; (**b**) shows curves of the normalized solar radiance calculated with roughness variance (σ^2) values of 0.003 and 0.01324 and the average measured radiance along the scan line, and the yellow box marks the position of the internal solitary waves. The blue and orange curves represent the radiance information of the sea surface background and internal solitary waves, respectively; (**c**) shows the changes in the solar zenith angle (θ_0), sensor zenith angle (θ), relative azimuth angle (ϕ), and surface facet tilt (β) along the AHI sensor scan line. The solid black line represents the change in the solar zenith angle (θ_0) along the scan line. The green dashed line represents the change in the sensor zenith angle (θ) along the scan line. The purple solid line represents the relative azimuth angle (ϕ) along the scan line. The blue dotted line represents the change in surface facet tilt (β) along the scan line.

To more clearly analyze the changes in the solar zenith angle (θ_0), sensor zenith angle (θ), and relative azimuth angle (ϕ) of the leading wave, Table 2 lists the solar zenith angle

(θ_0), sensor zenith angle (θ), and relative azimuth angle (ϕ) of the leading wave from 04:50–05:40 UTC on 21 September 2020.

Table 2. Three angles of the leading wave in consecutive images.

Time (UTC)	Solar Zenith Angle (θ_0)	Sensor Zenith Angle (θ)	Relative Azimuth Angle (ϕ)
2020-09-21-04:50	16.23°	23.70°	165.40°
2020-09-21-05:00	18.72°	23.74°	166.43°
2020-09-21-05:10	21.21°	23.78°	167.23°
2020-09-21-05:20	23.70°	23.82°	167.87°
2020-09-21-05:30	26.19°	23.86°	168.40°
2020-09-21-05:40	28.68°	23.90°	168.84°

In Table 2, the solar zenith angle (θ_0) increases because over time, the solar gradually moves westward and away from the study area. The sensor zenith angle (θ) also increases because the ISW packet propagates toward the southeast. The relative azimuth (ϕ) also increases, which is caused by the movement of the Sun and propagation of ISW packets. Every 10 min, the increases in the solar zenith angle (θ_0) and sensor zenith angle (θ) remain unchanged at 2.49° and 0.04°, respectively, while the relative azimuth angle (ϕ) increases gradually. The sensor zenith angle of the leading wave changes by approximately 0.20° within 50 min. The relative azimuth angle (ϕ) changes by approximately 3.44° within 50 min, and the solar zenith angle (θ) changes by approximately 12.45° within 50 min.

5. Discussion

According to the critical viewing angle theory, when the angle of internal waves is located on the left and right sides of the critical viewing angle, the bright and dark features of internal waves are the opposite. As shown in Figures 7–12, the sensor zenith angle (θ) of the leading wave changes by approximately 0.20° within 50 min, which is a very small change. The solar zenith angle (θ_0) of the leading wave changes by approximately 12.46° within 50 min, which is a very large change. Therefore, this paper attempts to explain this brightness reversal phenomenon, which is shown in Figure 5 based on the theory of the critical solar viewing angle.

As shown in Figures 7–12, the roughness variance (σ^2) values of the sea surface and the internal waves at the four moments are the same. Figure 13 shows a curve of the normalized sunglint radiance with the solar zenith angle (θ_0) when the sensor zenith angle (θ) is 23.80° and the relative azimuth angle (ϕ) is 166.73°, which are the average values of the six images, as listed in Table 2. The intersection points of the normalized sunglint radiance curves of the sea background and leading wave occur at 18.73° and 27.41°, respectively.

The solar zenith angle of the leading wave at 04:50 UTC is located on the left side of the intersection point of 18.73°, while the solar zenith angle of the leading wave at 05:10 UTC is located on the right side of the intersection point of 18.73°. According to the critical solar viewing angle theory, the bright and dark features of the leading wave at 04:50 UTC and 05:10 UTC are different, which is consistent with the phenomenon observed in Figure 5. The bright and dark features of the leading wave at 05:00 UTC are similar to those of the leading wave at 05:10 UTC because the solar zenith angle of the leading wave at 05:00 UTC is very close to the solar zenith angle of the leading wave at 05:10 UTC. The solar zenith angle of the leading wave at 05:30 UTC is located on the left side of the intersection point of 27.41°, while the solar zenith angle of the leading wave at 05:40 UTC is located on the right side of the intersection point of 27.41°. According to the critical solar viewing angle theory, the bright and dark features of the leading wave at 05:30 UTC and 05:40 UTC are different, which is consistent with the phenomenon observed in Figure 5.

Therefore, based on the calculated critical solar viewing angles (18.73° and 27.41°), the internal waves in the Celebes Sea, as observed in the Himawari-8 images, transition from a dark–bright pattern to a bright–dark–bright pattern and then back to the dark–bright pattern.

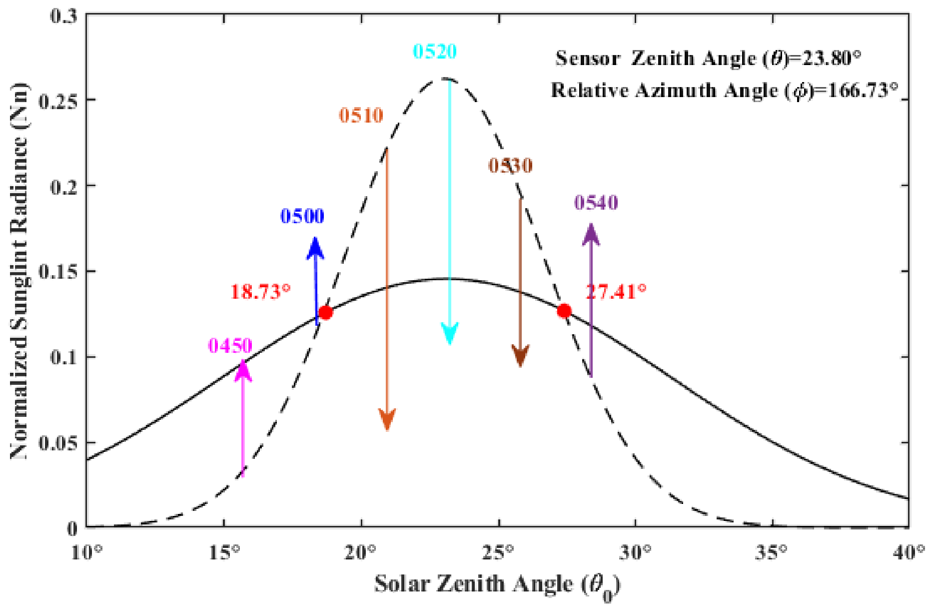

Figure 13. Curves of the normalized sunglint radiance (N_n) with the solar zenith angle (θ_0), where the sensor zenith angle (θ) remains fixed at 23.8° and the relative azimuth angle (ϕ) remains fixed at 166.73°. The roughness variance (σ^2) values of the sea surface and leading wave are 0.003 and 0.01324, respectively. There are two intersection points in the curves, i.e., the solar viewing angle (θ_{0c}). The pink arrow indicates that the solar zenith angle (θ_0) of the leading wave is 16.22° at 04:50 UTC, the blue arrow indicates that the solar zenith angle (θ_0) of the leading wave is 18.71° at 05:00 UTC, the orange arrow indicates that the solar zenith angle (θ_0) the leading wave is 21.21° at 05:10 UTC, the cyan arrow indicates that the solar zenith angle (θ_0) of the leading wave is 23.70° at 05:20 UTC, the brown arrow indicates that the solar zenith angle (θ_0) of the leading wave is 26.19° at 05:30 UTC, and the purple arrow indicates that the solar zenith angle (θ_0) of the leading wave is 28.68° at 05:40 UTC.

There are very few studies on the changes of the bright and dark features of internal waves, and it mainly analyzes the roles of the sensor zenith angle on the changes of the bright and dark features of internal waves. For example, Jackson analyzed the Andaman Sea image acquired by the Aqua satellite on 17 April 2003, and found that the bright and dark features of the two propagating solitary wave packets are in opposite patterns, and explained that the reason for this phenomenon is the existence of the critical sensor viewing angle [15]. Zhang discovered that the bright and dark features of the same internal wave near the Dongsha Islands detected by MODIS and OLCI are exactly opposite, mainly because of the OLCI camera turned 12.6° to the west [9]. Zhang used the experimental method to explain the existence of the critical viewing angle, and used the critical sensor viewing angle to explain two phenomena: the reversal of the bright and dark features of internal waves on the same image and the reversal of the bright and dark features of internal waves at the same position [8]. All these works illustrated the existence of critical perspectives and are applicable to all hotspot areas. According to the imaging mechanism of internal waves on optical remote sensing images, it is known that the critical sensor viewing angle exists, and the critical solar viewing angle may also exist. It is from this point that this article proves the existence of a critical solar perspective, which has never been discovered in existing studies.

Due to the limitation of data and time, this study has not discussed the existence of critical solar angle in other sea areas and under different conditions, which is also the direction of further research in the future.

6. Conclusions

Based on the sea surface normalized sunglint radiance and critical angle theories, this paper analyzes the process of brightness reversal of internal waves in six continuous Himawari-8 images.

In the brightness reversal process, internal waves first transition from a dark–bright pattern to a bright–dark–bright pattern and then back to the dark–bright pattern, which has never been reported in previous studies.

Based on the sea surface normalized sunglint radiance and critical sensor viewing angle theories, this paper expands the critical viewing angle theory and verifies the occurrence of the critical solar viewing angle.

Then, the solar zenith angle (θ_0), sensor zenith angle (θ), and relative azimuth angle (ϕ) of the leading wave are calculated in six continuous Himawari-8 images. The sensor zenith angle (θ) of the leading wave changes very little, at only approximately 0.20°, while the relative azimuth angle (ϕ) of the leading wave changes approximately 3.44°, and the change in the solar zenith angle (θ_0) of the leading wave reaches 12.45°.

Finally, this paper examines the role of the critical solar viewing angle in the brightness reversal process of internal waves based on Himawari-8 images. There are two critical solar viewing angles of 18.73° and 27.41°, which results in different bright and dark features of the ISWs when the solar zenith angle of the leading wave is located on the left and right sides, respectively, of the critical solar viewing angle.

The bright and dark features of internal waves in remote sensing images are related to sunglint in remote sensing images, which is inseparable from the solar zenith angle (θ_0), sensor zenith angle (θ), and relative azimuth angle (ϕ). Many results have been obtained in sensor zenith angle (θ) research regarding the reversal of the bright and dark features of internal waves [8,9,15]. In the future, it is necessary to further analyze the specific influence of the relative azimuth angle (ϕ), wind speed (W), and other factors on the brightness reversal process of internal waves.

Author Contributions: J.M. provided the conceptualization and revised the manuscript. B.H. developed the methodology, performed the experiments and analysis, and wrote the manuscript. L.S. discussed the analysis and revised the manuscript. H.Z. revised the manuscript. All authors have read and agreed to the published version of the manuscript.

Funding: This research was funded by the National Natural Science Foundation of China (No. 4200616).

Data Availability Statement: Supplementary data to this article can be found online at https://www.eorc.jaxa.jp/ptree/, accessed on 20 August 2021.

Acknowledgments: Authors would like to thank the Japanese Meteorological Agency (JMA) for providing the Himawari-8 data.

Conflicts of Interest: The authors declare no conflict of interest.

Abbreviations

There are many parameters in Sections 2 and 3. In this part, these parameters are listed in detail in order to better understand the idea of this paper, including concepts and calculation formulas.

Parameter	Definitions and Sources of Information
Lat	Latitude of the pixel
Lon	Longitude of the pixel
SatLat	Latitude of the sensor
SatLon	Latitude of the sensor
Ra	Real radiance of the pixel
P	Count of the pixel, which can be obtained from DAT file [29]
G	Gain for count-radiance conversion equation, which can be obtained from DAT file [29]

Parameter	Definitions and Sources of Information
C	Constant for count-radiance conversion equation, which can be obtained from DAT file [29]
N	The accumulated days arranged in the order of the number of days, which can be obtained from DAT file [29]
δ	Solar declination, which can be calculated by N [29]: $\delta = 0.006918 - 0.399912\cos\left(2\pi * \frac{N}{365}\right) + 0.010257\sin\left(2\pi * \frac{N}{365}\right) - 0.006758\cos 2\left(2\pi * \frac{N}{365}\right) + 0.000907\sin 2\left(2\pi * \frac{N}{365}\right)$
w	Solar hour angle, which can be calculated by N [29]: $w = 0.0172 - 0.4281\cos\left(2\pi * \frac{N}{365}\right) - 7.3515\sin\left(2\pi * \frac{N}{365}\right) - 3.4295cos2\left(2\pi * \frac{N}{365}\right) - 9.3619sin2\left(2\pi * \frac{N}{365}\right)$
R	Distances from the Earth center to the sensor, which can be obtained from DAT file [29]
D	Distances from the sensor to the pixel, which can be obtained from DAT file [29]
γ	Intermediate variable, which can be calculated by: $\gamma = arccos(cosLat\ cos(SatLon\text{-}Lon))$
β_1	Intermediate variable, which can be calculated by: $cos\beta_1 = cot\gamma tanLat$
ϕ_1	Solar azimuth angle, which can be calculated by: $\phi_1 = \arccos\left(\frac{\cos Lat\ sin\delta\ +\ sinLat\cos\delta\cos w}{\cos(90-\theta_0)}\right)$
θ_0	Solar zenith angle, which can be calculated by: $\theta_0 = arccos(cosLatcos\delta cosw + sinLat\ sin\delta)$
θ	Sensor zenith angle, which can be calculated by: $\theta = arcsin\left(\frac{R\ sin\gamma}{D}\right)$
ϕ	Relative azimuth angle, which can be calculated by: $\phi = \begin{cases} \beta_1 - \phi_1, & Lon - SatLon \le 0,\ Lat - SatLat < 0 \\ 180 - \beta_1 - \phi_1, & Lon - SatLon < 0,\ Lat - SatLat \ge 0 \\ 180 + \beta_1 - \phi_1, & Lon - SatLon \ge 0,\ Lat - SatLat > 0 \\ 360 - \beta_1 - \phi_1, & Lon - SatLon > 0,\ Lat - SatLat < 0 \end{cases}$
σ^2	Sea surface roughness variance which is related to wind speed
W	Wind speed
Z_{up}	Slope of the facet along the upwind direction
Z_{cr}	Slope of the facet along the crosswind direction
σ^2_{up}	Sea surface roughness variance along the upwind direction
σ^2_{cr}	Sea surface roughness variance along the crosswind direction
Z^2_x	Sea surface roughness variance along the x-axis direction
Z^2_y	Sea surface roughness variance along the y-axis direction
β	Surface tilt of a facet on the sea surface, which can be calculated by: $tan^2\beta = Z^2_x + Z^2_y$
$p(\theta, \theta_0, \phi, \sigma^2)$	Probability density function of the wave slope determining sunglint reflection, which can be be calculated by: $p(\theta, \theta_0, \phi, \sigma^2) = \frac{1}{2\pi\sigma^2}\exp\left(-\frac{1}{2}\left(\frac{tan^2\beta}{\sigma^2}\right)\right)$
L_0	The incident solar radiance on the sea surface
ω	Local reflection angle considering specular reflection of sunlight into the sensor by a facet thus tilted, which can be calculated by: $cos2\omega = cos\theta + cos\theta_0 + sin\theta_0 sin\theta cos\phi$
$\rho(\omega)$	Fresnel reflection coefficient for an unpolarized source, which can be calculated by: $\rho(\omega) = \frac{1}{2}\left(\frac{sin^2(\omega - r)}{sin^2(\omega + r)} + \frac{tan^2(\omega - r)}{tan^2(\omega + r)}\right)$
r	Angle of refraction for water, which can be calculated by: $\sin r = (sin\omega)/1.34$
L_{sg}	Glint radiance received by the sensor, which can be calculated by: $L_{sg} = \frac{L_0\rho(\omega)p(\theta,\theta_0,\phi,\sigma^2)}{4cos^2\beta cos\theta}$
$N(\theta, \theta_0, \phi, \sigma^2)$	Normalized sunglint radiance of the sea surface, which can be calculated by: $N(\theta, \theta_0, \phi, \sigma^2) = \frac{L_0}{L_{sg}} = \frac{\rho(\omega)}{4}p(\theta, \theta_0, \phi, \sigma^2)\frac{(1 + tan^2\beta)^2}{\cos\theta}$
θ_c	Critical sensor viewing angle
θ_{0c}	Critical solar viewing angle

References

1. Feng, S.Z.; Li, F.Q.; Li, S.J. *An Introduction to Marine Science*; Higher Education Press: Beijing, China, 1999; pp. 190–195.
2. Jiang, G.R.; Wang, X.J.; Zhang, J.; Zhang, R. The development of internal wave research at home and abroad. *Mar. Forecast.* **2005**, *22*, 176–182. [CrossRef]
3. Zheng, Q. Statistical and dynamical analyses of generation mechanisms of solitary internal waves in the northern South China Sea. *JGR-Oceans* **2007**. [CrossRef]
4. Alpers, W. Theory of radar imaging of internal waves. *Nature* **1985**, *314*, 245–247. [CrossRef]
5. Mitnik, L.; Alpers, W.; Chen, A.J. Manifestation of internal solitary waves on ERS SAR and SPOT images: Similarities and differences. In Proceedings of the 2000 International Geoscience and Remote Sensing Symposium (IGARSS'00), Honolulu, HI, USA, 24–28 July 2000; pp. 1857–1859. [CrossRef]
6. Melsheimer, C.; Kwoh, L.K. Sun glitter in SPOT images and the visibility of oceanic phenomena. In Proceedings of the 22nd Asian Conference on Remote Sensing, Singapore, 5–9 November 2001.
7. Ho, C.R.; Su, F.C.; Kuo, N.J. Internal wave observations in the northern South China Sea from satellite ocean color imagery. *Int. J. Remote Sens.* **2008**, *29*, 6373–6380. [CrossRef]
8. Zhang, M.; Wang, J.; Chen, X. An experimental study on the characteristic pattern of internal solitary waves in optical remote-sensing images. *Int. J. Remote Sens.* **2019**, *40*, 7017–7032. [CrossRef]
9. Zhang, X.D.; Zhang, J.; Meng, J.M. Observation of internal waves with OLCI and SRAL on board Sentinel-3. *Acta Oceanologica Sinica* **2020**, *39*, 56–62. [CrossRef]
10. Cox, C.; Munk, W. Measurement of the Roughness of the Sea Surface from Photographs of the Sun's Glitter. *J. Opt. Soc. Am.* **1954**, *44*, 838–850. [CrossRef]
11. Saunders, P.M. Radiance of Sea and Sky in the Infrared Window 800–1200 cm^{-1}. *J. Opt. Soc. Am.* **1968**, *58*, 645–652. [CrossRef]
12. Chapman, R.D. Visibility of rms slope variations on the sea surface. *Appl. Opt.* **1981**, *20*, 1959–1966. [CrossRef]
13. Zeisse, C.R. Radiance of the ocean horizon. *J. Opt. Soc. Am. A* **1995**, *12*, 99. [CrossRef]
14. Matthews, J. Stereo observation of lakes and coastal zones using ASTER imagery. *Remote Sens. Environ.* **2005**, *99*, 16–30. [CrossRef]
15. Jackson, C.; Alpers, W. The role of the critical angle in brightness reversals on sunglint images of the sea surface. *J. Geophys. Res.* **2010**, *115(C9)*. [CrossRef]
16. Zhang, X.D. Study on Amplitude Inversion of Internal Waves Based on the Schrödinger Equation and Multi-Source Remote Sensing Data. Ph.D. Thesis, Ocean University of China, Qingdao, China, 21 March 2018.
17. Turiel, A.; Isern-Fontanet, J.; Garcia-Ladona, E. Detection of wave fronts in the Indian Ocean from geostationary sunglint satellite imagery. *Int. J. Remote Sens.* **2007**, *28*, 3953–3962. [CrossRef]
18. Lindsey, D.T.; Nam, S.H.; Miller, S.D. Tracking oceanic nonlinear internal waves in the Indonesian seas from geostationary orbit. *Remote Sens. Environ.* **2018**, *208*, 202–209. [CrossRef]
19. Gao, Q.; Dong, D.; Yang, X. Himawari-8 Geostationary satellite observation of the internal solitary waves in South China Sea. In Proceedings of the 2018 ISPRS TC III Mid-term Symposium "Developments, Technologies and Applications in Remote Sensing", Beijing, China, 7–10 May 2018; pp. 363–370. [CrossRef]
20. Karang, I.; Chonnaniyah, N.; Osawa, T. Internal solitary wave observations in the Flores Sea using the Himawari-8 geostationary satellite. *Int. J. Remote Sens.* **2019**, 1–17. [CrossRef]
21. Ma, Z.D.; Meng, J.M.; Sun, L.N.; Liu, Y.X. Observation of internal waves in the ocean using FY-4A meteorological satellite. *Mar. Sci.* **2021**, *45*, 32–39. [CrossRef]
22. Sprintall, J.; Gordon, A.L.; Koch-Larrouy, A. The Indonesian Seas and their impact on the Coupled Ocean-Climate System. *Nat. Geosci.* **2014**, *7*, 487. [CrossRef]
23. Devantier, L.; Wilkinson, A.C. The Sulu-Sulawesi Sea: Environmental and Socioeconomic Status, Future Prognosis and Ameliorative Policy Options. *Ambio* **2004**, *33*, 88–97. [CrossRef] [PubMed]
24. Liu, B.; D'Sa, E.J. Oceanic Internal Waves in the Celebes Sea Under Sunglint and Moonglint. *IEEE Trans. Geosci. Remote Sens.* **2019**, *57*, 6119–6129. [CrossRef]
25. Zhang, T.; Zhang, X.D. Characteristics on internal solitary waves in the Sulu-Celebes Sea based on MODIS and VIIRS remote sensing images. *Oceanol. Limnol. Sin.* **2020**, *51*, 29–38.
26. Sun, L.N.; Zhang, J.; Meng, J.M. Analysis of Spatio-Temporal Distribution of Internal Solitary Waves in the South China Sea and Sulu Sea (2010–2015). *Adv. Mar. Sci.* **2019**, *37*, 398–408.
27. He, X.W.; Feng, X.H.; Han, Q.; Zhang, J.S.; Zhao, X.G. The Characteristics Study of the New Generation of Geostationary Meteorological Satellite Imager. *Softw. Guide* **2019**, *18*, 140–143. [CrossRef]
28. Bessho, K.; Date, K.; Hayashi, M. An introduction to Himawari-8/9-Japan's new-generation geostationary meteorological satellites. *Meteorol. Soc. Jpn.* **2016**, *94*, 151–183. [CrossRef]
29. HANS. *Himawari-8/9 Himawari Standard Data User's Guide*; Japan Meteorological Agency: Tokyo, Japan, 2015; pp. 2–3.
30. Tan, X.S.; Ge, C.H. A method for calculating solar angles and its application on remote sensing. *Remote Sens. Land Resour.* **1995**, *2*, 48–57. [CrossRef]
31. Reda, I.; Andreas, A. Solar position algorithm for solar radiation applications. *Sol. Energy* **2004**, *76*, 577–589. [CrossRef]